Cross-Validation of Hybrid-Electric Aircraft Sizing Methods

Finger, D. Felix; de Vries, Reynard; Vos, Roelof; Braun, Carsten; Bil, Cees

DOI
10.2514/1.C035907

Publication date
2022

Document Version
Final published version

Published in
Journal of Aircraft

JOURNAL OF AIRCRAFT
Vol. 59, No. 3, May–June 2022

Cross-Validation of Hybrid-Electric Aircraft Sizing Methods

D. Felix Finger*
FH Aachen University of Applied Sciences, 52064 Aachen, Germany
Reynard de Vries† and Roelof Vos‡
Delft University of Technology, 2629HS Delft, The Netherlands
Carsten Braun§
FH Aachen University of Applied Sciences, 52064 Aachen, Germany
and
Cees Bil¶
RMIT University, VIC 3000 Melbourne, Australia

https://doi.org/10.2514/1.C035907

The number of studies on hybrid-electric aircraft is steadily increasing because these configurations can lead to lower operating costs and environmental impact than traditional aircraft. However, due to the lack of reference data of actual hybrid-electric aircraft, the design tools and results are difficult to validate. This paper analyzes the key points that must be validated when developing or implementing a hybrid-electric aircraft design tool by contrasting the assumptions and results of two independently developed sizing methods. An existing 19-seat commuter aircraft is selected as the baseline test case, and both design tools are used to size that aircraft. The aircraft is then resized under consideration of hybrid-electric propulsion technology. This is performed for parallel, serial, and fully electric powertrain architectures. Finally, sensitivity studies are conducted to assess the validity of the basic assumptions and approaches regarding the design of hybrid-electric aircraft. Both methods are found to predict the maximum takeoff mass (MTOM) of the reference aircraft with less than 4% error. The MTOM and payload-range energy efficiency of various (hybrid-) electric configurations are predicted with a maximum difference of approximately 2 and 5%, respectively. The results of this study confirm a correct formulation and implementation of the two methods and provide a reference data set that can be used to benchmark design tools.

Nomenclature

A	=	aspect ratio
C_D	=	drag coefficient, $D/(0.5\rho_\infty V_\infty^2 S)$
$C_{D,\min}$	=	minimum drag coefficient
C_L	=	lift coefficient, $L/(0.5\rho_\infty V_\infty^2 S)$
$C_{L\,\max}$	=	maximum lift coefficient
$C_{L,\min D}$	=	minimum-drag lift coefficient
D	=	drag, N
E	=	energy, J
E^*	=	specific energy, J/kg or W · h/kg
e	=	Oswald's aircraft efficiency factor
H_P	=	hybridization ratio
h	=	altitude, m
k	=	induced drag factor
L	=	lift, N
L/D	=	lift-to-drag ratio
M	=	Mach number
m	=	mass, kg
P	=	power, W
P^*	=	specific power, kW/kg
P/W	=	power-to-weight ratio, W/N
p	=	pressure, Pa
R	=	range, km
Re	=	Reynolds number
S	=	wing reference area, m^2
T	=	thrust, N
V	=	velocity, m/s
V_s	=	stall speed, m/s
W	=	weight, N
W/P	=	power loading, N/W
W/S	=	wing loading, N/m^2
y^+	=	nondimensional wall distance
α	=	angle of attack, deg
$\Delta(\ldots)$	=	change in aerodynamic property
η	=	efficiency
μ	=	dynamic viscosity, Pa · s
ρ	=	density, kg/m^3
Φ	=	supplied power ratio

Subscripts

bat	=	battery
cr	=	cruise
div	=	diversion
EM	=	electrical motor or machine
f	=	fuel
GB	=	gearbox
GEN	=	electrical generator
GT	=	gas turbine
miss	=	nominal mission (excluding reserves)
OEM	=	operating empty mass
OEM′	=	operating empty mass without propulsion system
PH	=	parallel hybrid
PL	=	payload
p	=	propulsive
s	=	shaft
SH	=	serial hybrid

Presented as Paper 2020-1006 at the AIAA SciTech 2020 Forum, Orlando, FL, January 6–10, 2020; received 6 February 2020; revision received 9 September 2021; accepted for publication 20 December 2021; published online 8 February 2022.

*Lecturer, Department of Aerospace Engineering; f.finger@fh-aachen.de. Member AIAA.
†Ph.D. Candidate, Faculty of Aerospace Engineering; r.devries@tudelft.nl. Student Member AIAA.
‡Assistant Professor, Faculty of Aerospace Engineering; r.vos@tudelft.nl. Associate Fellow AIAA.
§Professor, Department of Aerospace Engineering; c.braun@fh-aachen.de. Member AIAA.
¶Professor, School of Engineering; cees.bil@rmit.edu.au. Associate Fellow AIAA.

SL = sea level
TO = takeoff
∞ = freestream conditions

I. Introduction

THE reduction of greenhouse gases is a relevant topic in every field of today's research. For land-, water-, and air-based traffic, electric propulsion is a potential solution to achieve a reduction in emissions and minimize the use of fossil fuel. Fully electric cars and ships are already in mass production (see, e.g., Refs. [1,2]), but only a small number of experimental aircraft currently use electric propulsion. This is mainly due to the current battery technology, which limits flight endurance and range [3]. Until battery technology is mature enough [4], hybrid-electric powered aircraft could help to reduce emissions, fuel burn, and noise. Interest in hybrid-electric aircraft design has significantly increased, as shown by the growing number of publications on this topic [5]. However, design procedures and best practices for hybrid-electric aircraft are yet to be developed [6]. In this context, one of the main challenges is the initial sizing of hybrid-electric aircraft, that is, the process of going from the first concept to a baseline design with component masses and engine power that reflect the top-level aircraft requirements.

Many studies are conducted exploring the design space of this new technology. Some studies retrofit an existing aircraft with hybrid-electric propulsion (HEP) to analyze a specific aspect of the technology, maintaining takeoff mass constant (e.g., Refs. [7–9]). Others actively resize the aircraft to allow a fair comparison with a conventional reference aircraft (e.g., Refs. [10–14]). However, these studies often lack transparency regarding the aircraft sizing process. Furthermore, the results of hybrid-electric design studies are usually—if not always—presented without any validation or uncertainty quantification, despite the use of novel design methods. This can, at least partly, be attributed to the fact that validation and verification of design tools for hybrid-electric aircraft is a very challenging task due to the lack of available validation data. On the one hand, validation data from existing design studies are scarce because most research does not explicitly list assumptions or provide sufficient quantitative data to replicate the designs. On the other hand, given that hybrid-electric propulsion is an emerging technology, there are only a very limited number of manned hybrid-electric aircraft that have been flight tested. Examples of hybrid-electric aircraft include a modified ultralight aircraft built by the University of Cambridge [15], a retrofitted Cessna 337 by Ampaire,[**] and a modified DA40 built by Diamond Aircraft.[††] Because all these aircraft are experimental or prototypes with hybrid-electric propulsion systems retrofitted to existing conventional aircraft, they are not representative of a fully optimized clean-sheet design and, moreover, only a limited amount of data is publicly available.

The purpose of this paper is, therefore, to present a benchmark study for the validation of hybrid-electric aircraft sizing methods. To this end, a detailed qualitative and quantitative comparison of two independently developed sizing routines is performed. The assumptions, discrepancies, and results provided by the two methods are discussed in order to maximize transparency. This comparison supports the validation process of hybrid-electric aircraft sizing for two reasons. Firstly, it exposes which key aspects of the sizing process require an explicit validation because they are not present in traditional sizing methods. Secondly, it provides a series of input and output values that can serve as a reference data set to benchmark other design methods.

To achieve this, first, the reasoning behind the validation process is presented in Sec. II. Then, the two sizing methods are briefly described in Sec. III, highlighting the differences between them. These two methods are subsequently used to size a baseline aircraft for a common set of top-level requirements and a conventional turboprop propulsion system, as described in Sec. IV. Then, hybrid-electric propulsion technology is introduced in Sec. V. Both methods are used to resize the aircraft under consideration of serial, parallel, and fully electric propulsion system architectures. To verify that the trends of the different approaches match, a sensitivity study is conducted. With this, the gradient of any figure of merit with regard to the analyzed parameters can then be determined, illustrating the impact of each parameter on the final design and showcasing the differences between both methods. In this way, the study presented in this paper helps to build confidence in the design methods for hybrid-electric aircraft and to understand the impact that hybrid-electric propulsion systems have on the initial sizing process.

II. Approach to the Validation Procedure

A formal validation process for entire design methods does not exist to the knowledge of the authors. In this sense, aircraft sizing methods are very different from other software tools developed in the aerospace field. Aerodynamic solvers, for example, are often computationally complicated but conceptually simple, in the sense that they analyze a single discipline with its associated physical laws. The set of governing equations, the impact of temporal and special discretization, and the treatment of boundary and initial conditions are generally well understood, and formal validation and verification techniques can be applied. In simple cases, it is possible to derive analytical solutions for comparison. In others, it is possible to create a data set for validation by performing an experiment with a subcomponent or scaled-down version of the aircraft.

In contrast, sizing methods are computationally inexpensive but conceptually complex. Because these tools integrate different disciplines—often modeled in a highly simplified manner—errors are extremely hard to pinpoint. For a reference airplane with known characteristics, an error in absolute fuel burn could be attributed to an incorrect mass model, an incorrect propulsion model, or an incorrect aerodynamics model. Consequently, design methods are generally broken down into parts and submodules, which are, in turn, verified and validated individually. However, this alone is not sufficient, because these parts must also be appropriately selected and integrated, such that the most important dependencies are accounted for. To confirm this, a validation of the complete design tool is required. For conventional configurations, it is possible to perform the sizing of several real-world aircraft and gain experience with the tool, Then, accuracy and applicability can be judged. Without any real-world reference, as is the case for aircraft employing hybrid-electric propulsion, this is not an option.

Therefore, the next best approach to the validation problem is to benchmark independent methods against each other. Although this provides no formal proof of the accuracy of the methods, it increases the confidence that the methods are reliable if they independently 1) provide (almost) the same results for the same input parameters, and 2) have (almost) the same sensitivity to a change in the input parameters. To maximize this confidence in the sizing methods, the impact of the parameters that have the largest influence on the aircraft figures of merit, or those that present the largest uncertainty, should be analyzed. Although the influence of each parameter depends on the configuration, for any hybrid-electric aircraft sizing tool, at least the following three sets of parameters should be considered:

Firstly, the aircraft must be sized for different mission requirements. Previous studies have indicated that hybrid-electric propulsion presents the greatest benefits for missions that are typically not covered by conventional aircraft; for example, fully electric configurations are only efficient for very short ranges [3], whereas turboelectric configurations are beneficial for very long ranges [16]. To be able to conclude which configuration is best for a determined set of mission requirements, it is essential first to verify that the sizing method produces accurate results independently of the type of mission considered. Moreover, it is easy to adapt the aerodynamic

**N. Zazulia, "Hybrid-Electric Cessna 337 Takes Maiden Flight," Avionics International, 6 June 2019, http://www.aviationtoday.com/2019/06/06/ampaire-hybrid-electric-cessna-flight/.

††A. M. Lentsch, "Diamond Aircraft 1st Flight Multi-Engine Hybrid Electric Aircraft," 7 November 2018, http://www.diamond-air.at/en/media-center/press-releases/news/article/diamond-aircraft-1st-flight-multi-engine-hybrid-electric-aircraft/.

assumptions or propulsion-system characteristics such that the desired output values (e.g., fuel weight of the reference aircraft) are obtained for a determined set of mission requirements. This can be done on purpose or can occur unintentionally. To minimize this bias, it is necessary to chart the aircraft figures of merit for multiple mission requirements.

Secondly, it is important to verify the sensitivity of the sizing method to the technology-level assumptions made for the hybrid-electric powertrain components. A common example is the sensitivity to battery energy density or power density. Typically, values way beyond the state-of-the-art are assumed [11]. Not only do these projections have a large uncertainty, but additionally they have a very large impact on the aircraft figures of merit.

Thirdly, the effect of HEP design parameters, such as the power split between the two energy sources, must be analyzed. Depending on the formulation of the method, this design choice can be either a scalar (such as the degree of hybridization [17]), or a time-dependent control variable (such as the supplied power ratio [18]). In both cases, if the results of a hybrid configuration do not tend to those of a fully fuel-based or electric configuration in the limits of "zero percent hybridization" and "hundred percent hybridization," respectively, then the effects of discrete design choices such as the powertrain architecture are not properly accounted for.

Based on these considerations, the validation procedure outlined in Fig. 1 is used to cross-validate the two HEP sizing methods. The first step in this validation process is the validation of each of the analysis methods that are embedded in the submodules. These include weight estimation methods and the estimation of drag polar of the aircraft. As will be evident in the following section, both methods rely on previously validated weight estimation methods (see, e.g., Ref. [19]), and therefore their validation is not repeated in this paper. The aerodynamic model used to obtain an estimate of the drag polar, which is described in Sec. IV.B, also has been validated in earlier studies (Refs. [20,21]) and is therefore not included here.

The second step is assessing whether the integration of the submodules in the overall sizing routine leads to a correctly sized aircraft, whose figures of merit can be compared with existing data. In this "reverse-engineering" step, the input to the sizing method is obtained from reference data as well. This includes, but is not limited to, data on the aircraft performance, i.e., mission range, takeoff field length, landing distance, maximum payload weight, maximum passenger capacity, etc. Once both the sizing methods have been independently validated for conventional aircraft with benchmark data, the third step is to include hybrid-electric configurations and compare the predicted figures of merit of each method with each other. For this cross-validation, different HEP powertrain configurations are evaluated in the following sections, and the takeoff mass and payload-range energy efficiency are compared. These figures of merit are selected for comparison because they depend on all input parameters, and thus any significant difference in the sizing method should be reflected in these parameters.

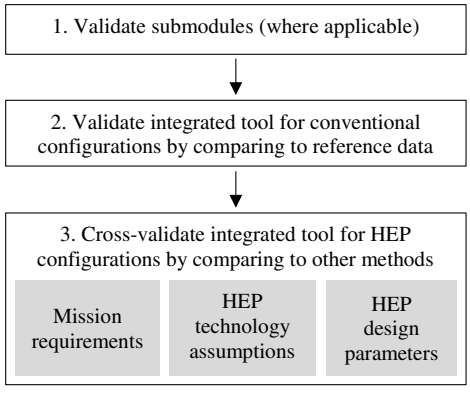

Fig. 1 Main steps of the validation procedure.

III. Sizing Methods

At FH Aachen and TU Delft, sizing tools for hybrid-electric aircraft have been independently developed in parallel over the past years. In both approaches, the traditional preliminary sizing methods [22–29] were modified to account for hybrid-electric propulsion. The method developed at FH Aachen focuses on the design of general aviation aircraft with special emphasis on vertical takeoff and landing (VTOL). The approach of TU Delft focuses on the design of transport aircraft with special focus on the aeropropulsive effects associated with distributed-propulsion or boundary-layer-ingestion configurations.

In this section, the design methods of FH Aachen (Sec. III.A) and TU Delft (Sec. III.B) employed to create a benchmark are briefly described. The main differences between the two methods are then summarized in Sec. III.C. Finally, Sec. III.D describes the simplified powertrain representations and parameterizations used by the two methods.

A. Method A: FH Aachen

The design methodology formulated at FH Aachen was conceived for the design of general aviation aircraft. Special focus was put on the ability to analyze VTOL aircraft. The methodology of the sizing process is documented in Ref. [17]. Conventional takeoff and landing general aviation aircraft were studied, as shown in Refs. [30–34]. The sizing of VTOL aircraft is discussed in Ref. [35]. The FH Aachen method is developed for aircraft with both parallel-hybrid and serial-hybrid propulsion systems, although it is applicable to conventional propulsors or fully electric propulsion systems as well. Therefore, the algorithm can be integrated into existing design or analysis tools. Its goal is the identification of the optimal design point (P/W_{TO} and W_{TO}/S) of such aircraft and, in addition to this, the corresponding degree of hybridization. Analogous to the classical methods, the methodology is separated into two major parts: point performance, also referred to as the constraint diagram, and mission performance, also known as the mass estimation. For both parts, certain input parameters are necessary, representing the top-level aircraft performance requirements (TLARs), which are defined for the individual aircraft. These requirements specify the TLARs, including the flight mission, the aerodynamics, and the propulsion system (number of engines, conventional, serial- or parallel-hybrid, etc.) and its corresponding efficiencies. The mission is broken into a large number of short segments and simulated, using an energy-based approach. To cover the mix of consumable (fuel) and nonconsumable (batteries) energy sources, the masses are not treated as fractions, but as absolute values. Based on a first estimate for the maximum takeoff mass (MTOM), all masses that make up the gross mass are calculated. This can be done by using class I or class II mass estimation methods from Refs. [22,23,28,29]. Based on the new MTOM, the next iteration step can be started.

B. Method B: TU Delft

The methodology developed at TU Delft focuses on the preliminary sizing of hybrid-electric transport aircraft, taking into account the aeropropulsive interaction effects present in novel propulsion-system layouts such as distributed propulsion, tip-mounted propulsion, or boundary-layer ingestion systems. The sizing process is documented in Ref. [18] and has been used in both configuration studies [36–39] and sensitivity studies [16,18]. Analogously to the approach of FH Aachen, the sizing method combines a point-performance analysis with a mission analysis and subsequent mass estimation. The main advantages of the method developed by TU Delft are the inclusion of aeropropulsive interaction in the sizing process, and the use of a generic powertrain model that is independent of the type of architecture selected. The main disadvantages, on the other hand, are that the method is not applicable to VTOL and that it requires a more complex representation of the design space due to the use of multiple power-loading diagrams. This difference will be discussed in more detail in Sec. V.

In this method, the point-performance equations of the aircraft are modified to include the changes lift, drag, and propulsive due

to aeropropulsive interaction effects. Once the constraint diagram has been established in terms of the required propulsive power ($P_p = T \cdot V$), a simplified matrix representation of the powertrain is used to relate the propulsive power to the power required from the energy sources and the different components of the powertrain. A time-stepping mission analysis then is performed to size the aircraft in terms of energy requirements. The resulting fuel and battery masses are included in a modified class I mass breakdown of the aircraft, and the MTOM is computed. With this updated MTOM, the mission analysis is re-evaluated until the aircraft mass converges.

C. Differences Between Sizing Methods

Although both methods A and B stem from the well-known class I design methods, slightly different results must be expected due to differences in assumptions or modeling approaches. Different models are used for the constraint analysis (shown in more detail in Figs. 7 and 10), the mission analysis, and the systems analysis, with each model having individual strengths and weaknesses. To provide an overview, Table 1 highlights the key differences between methods A and B. For a more complete understanding of the rationale behind the two methods, the reader is referred to Refs. [17,18].

Both methods use the constraint diagram, also known as the "matching chart," to derive the installed power. However, the main difference between the two methods is the use of a single, combined power-loading diagram in method A, versus the use of multiple component-oriented power-loading diagrams in method B. Consequently, method A assumes a specific power split for all constraints, whereas method B is more flexible but requires the designer to select a power split (i.e., a supplied power ratio; see Sec. III.D) for each constraint. The two approaches are described in detail when analyzing these diagrams for a hybrid-electric aircraft in Sec. V.B. Moreover, a slightly different approach is used to determine the takeoff and climb rate constraints. To determine the relationship between power, wing loading, and takeoff distance, method A solves an analytic equation from Gudmundsson [25], which takes into account aircraft drag and rolling friction. Method B uses a statistical approach based on $C_{L,\mathrm{TO}}$, as described by Raymer [22]. To derive the climb-rate constraints, the same approach is used to find excess power; however, climb is performed at different speeds. Method A derives the speed for minimum drag power (maximum) $C_L^{3/2}/C_D$, whereas method B assumes a stall margin of $1.2V_S$, because it is not possible to analytically derive the optimum climb speed when the aeropropulsive interaction effects are considered.

The same difference is reflected in the mission analysis, where method A accelerates to the speed of minimum drag power, climbs, levels off at the desired altitude, and then accelerates to cruise speed. Method B, on the other hand, climbs at constant dM/dh, which leads to a smooth climb profile, but is less energy efficient. A dM/dh profile is assumed for descent as well, at an idle throttle setting of 5%, for which the thrust produced is included in the point-performance equations. Method A handles descent more conservatively: a 10% throttle setting is considered as idle, but no residual thrust is considered during descent. In this case, the descent speed is adjusted to the velocity for best L/D. The taxi, takeoff, and landing flight phases are also handled differently. Method A simulates the energy consumption of taxi phases by considering rolling friction, the taxi time and speed, and the takeoff energy consumption by applying full power for a determined duration. The landing phase is considered part of the postlanding taxi. Method B covers these flight phases by using Roskam's energy fractions [27], where statistical data are used to describe that part of the mission. In this study, the energy fractions assumed in method B were selected to match the energy fractions computed in method A. Furthermore, the fuel reserves required for loiter are computed in a different manner, as shown in Table 1.

Because method A was developed for reciprocating engines, as they are typically found for general aviation, turboprop efficiency is described by brake-specific fuel consumption (BSFC) values. Method B, on the other hand, describes gas turbine thermal efficiency directly, using the factor η_{GT}. In both cases, the turboshaft efficiency is throttle (part-power) corrected, using an empirical formula for jet engines, as described in Ref. [22]. To prevent efficiency from reaching zero at 0% throttle, the BSFC values of method A have a certain maximum cutoff, whereas the efficiency is considered constant below 15% throttle by method B.

Finally, to model the operating empty mass (OEM), both methods use statistical class I mass estimation methods for this comparison, even though class II methods from Refs. [22,23,28,29] are implemented in method A. However, method A defines OEM′ as the OEM without a propulsion system. The propulsion system mass is added separately, to account for the large propulsion systems of VTOL aircraft, which are not covered by the typical statistical correlations. Method B considers a conventional OEM definition, but corrects it to account for the increased powertrain weight. In this comparative

Table 1 Summary of the main differences between the two sizing methods

Modeling approach	Method A	Method B
Loading diagram: Design-point selection	Single shaft-power diagram, relative size of components determined by power split	One diagram per component; size of each component determined in respective diagram
Loading diagram: Powertrain parameterization	Hybridization of installed power, H_{P}, applied simultaneously to all constraints in loading diagram	Supplied power ratio, Φ, specified for each constraint in loading diagram
Loading diagram: Takeoff constraint	Gudmundsson's method, modified for offset drag polar (sensitive to drag and rolling friction)	Raymer's takeoff parameter
Loading diagram: Climb rate constraints	Performed at minimum drag power, $C_L^{3/2}/C_D$	Performed with a stall margin, $V = 1.2V_{\mathrm{s}}$
Mission analysis: Taxi	Given taxi time and taxi speed, rolling friction must be overcome	Fuel/energy fractions
Mission analysis: Takeoff/ landing	Assume x minutes at a determined throttle setting	Fuel/energy fractions
Mission analysis: climb strategy	Climb at $C_L^{3/2}/C_D$ and then accelerate to cruise speed	Constant $\mathrm{d}M/\mathrm{d}h$; leads to smooth profile but slightly higher energy consumption
Mission analysis: descent strategy	10% throttle (∼ idle), which consumes energy but produces no thrust; descent at best L/D speed	5% throttle (∼ idle), which produces some residual thrust
Mission analysis: Loiter	x minutes at constant altitude and flight speed, including transients to reach loiter speed and altitude	x minutes at constant altitude and optimum flight speed in terms of energy consumption; transients neglected
Turboprop/ Turboshaft efficiency	Constant above a given BSFC value	Constant below a given throttle setting
OEM/MTOM fraction	OEM′/MTOM = 0.545;OE′ excludes powertrain	OEM/MTOM = 0.600;OEM includes powertrain

study, a constant empty-mass fraction is used for the reference aircraft. For the Do 228 data (OEM/MTOM = 0.609), statistics from Ref. [22] give an OEM/MTOM of approximately 0.6, with a decreasing trend with increasing MTOM. Statistics from Ref. [25] also give an OEM/MTOM of approximately 0.6, with an increasing trend with increasing MTOM. The sensitivity of the OEM fraction to MTOM was found to be small for the commuter class in both cases, and therefore a constant empty-mass fraction of OEM/MTOM = 0.600 was selected for method B, and an equivalent mass fraction of OEM′/MTOM = 0.545 for method A, which corresponds to the same value if the propulsion-system mass of the Do 228 is subtracted.

D. Hybrid-Electric Powertrain Definitions

Multiple different powertrain architectures can be conceived when considering (hybrid-) electric propulsion [40]. Different levels of modeling detail exist, depending on the focus of the design study. In the preliminary sizing methods treated in this paper, a simplified model is used where each component is treated as a "black box" with an associated weight and transmission efficiency. Although a more complete description of these simplified representations can be found in Refs. [18,41], a brief overview of the serial and parallel architectures is included here for clarity, to relate the different parameterizations of the two methods to each other.

The parallel hybrid architecture (Fig. 2a) is a configuration in which gas turbine (GT) and electric motor (EM) work in conjunction. Both are mechanically connected to a propeller shaft, often via a gearbox. The total required power is split between GT and EM by a certain degree of hybridization. In a serial-hybrid system (Fig. 2b) the propulsor shaft is only driven by an EM, whereas the GT is used to generate electricity for the electric system. The electric system is supplemented by a battery.

Serial architectures enable distributed propulsion layouts (see, e.g., Refs. [42–44]), which enhance the aeropropulsive efficiency of the aircraft. Thereby, the mass increase of the propulsion system is traded against improved aerodynamic efficiency. However, in this paper, aeropropulsive effects are not considered, to simplify the analysis and improve comparability. Parallel and serial powertrains have a mechanical and electrical node, respectively. Therefore, when compared with a conventional fuel-burning powertrain, additional degrees of freedom are available. Method A uses the parameter H_P to describe the hybridization. H_P is the level of hybridization of power, which for parallel architectures is the ratio of the propulsion power of EMs to the total propulsion power at the propeller shaft [see Eq. (1)]. Note that for serial hybrid-electric powertrains, $H_{P,PH}$, as defined in Eq. (1), is always equal to one because only the EM delivers the total installed power. To differentiate between the fully electric powertrain and to size the generator, in this case, the parameter $H_{P,SH}$, is introduced by Eq. (2).

$$H_{P,PH} = \frac{P_{EM}}{P_{EM} + P_{GT}} \tag{1}$$

$$H_{P,SH} = \frac{P_{bat}}{P_{bat} + P_{GEN}} \tag{2}$$

This definition of $H_{P,SH}$ is different from the definition provided in Ref. [17]. Previous publications defined $H_{P,SH}$ as the ratio between P_{EM} and P_{GT}. This definition would result in a hybridization ratio of less than 1 for parallel hybrids, and larger than 1 for serial hybrids. For the sake of comparability, the definition is changed for this paper, so that the ratio H_P is less than 1 for both SH and PH, which makes it similar to the hybridization definition of method B.

Method B, on the other hand, uses the *supplied power ratio*, which can be expressed as

$$\Phi = \frac{P_{bat}}{P_{bat} + P_f} \tag{3}$$

Although this parameter governs the power split at the node (i.e., the gearbox for the parallel architecture, or the electrical node for the serial architecture), in this case, the supplied power ratio specifies the value of the split at the energy sources rather than at the node itself, unlike the parameter H_P. This formulation is necessary to apply the generalized matrix formulation used to solve the different powertrain architectures, as described in Ref. [18]. Because the definition of the two control variables differs only by the transmission efficiency of the components located between the energy sources and the nodes, they can easily be related to each other through:

$$\Phi = \begin{cases} \dfrac{1}{1 + \frac{\eta_{EM}}{\eta_{GT}} \frac{(1-H_{P,PH})}{H_{P,PH}}}, & \text{for parallel architectures} \\ \dfrac{1}{1 + \frac{1}{\eta_{GT}\eta_{GEN}} \frac{(1-H_{P,SH})}{H_{P,SH}}}, & \text{for serial architectures} \end{cases} \tag{4}$$

In both formulations, a fully electrical powertrain is achieved if the power split is equal to one ($H_P = 1 \leftrightarrow \Phi = 1$) for all mission segments and performance constraints of the sizing process. In that case, the power required from the gas turbine is zero independently of the architecture considered. Therefore, in both sizing methods, the fully electrical architecture can automatically be obtained as a limit case of architectures shown in Fig. 2.

IV. Baseline Reference Aircraft

In this section, a baseline reference aircraft is sized for a given set of top-level requirements. For this study, a 19-seat, CS-23 commuter aircraft is selected. Commuter-class aircraft (up to 8618 kg) are larger than the general aviation category (up to 5760 kg), for which method A is designed, and smaller than the CS-25 transport aircraft, for which method B is typically used. In this way, it is possible to verify that the approaches are generic enough for the sizing of hybrid-electric aircraft in general, and not just limited to the aircraft category for which they were initially intended. The results are subsequently used as a baseline for the hybridization studies of Sec. V.

A. Definition of Top-Level Aircraft Requirements and Design Assumptions

The reference aircraft is based closely on the Dornier/RUAG Do 228NG, a twin-turboprop short take-off and landing (STOL) utility aircraft [45]. This aircraft has been analyzed in previous hybrid-electric aircraft studies (see, e.g., Refs. [7,46]). Moreover, performance data of the aircraft are available from multiple sources [47–50], and therefore it is well-suited as a reference configuration. The Do 228 is built in conventional aluminum construction and features a high wing and a rectangular-shaped fuselage. The fuselage is not pressurized. The landing gear retracts into a fuselage pod. For propulsion, Honeywell TPE331 engines are used. They are flat-rated to 579 kW when installed

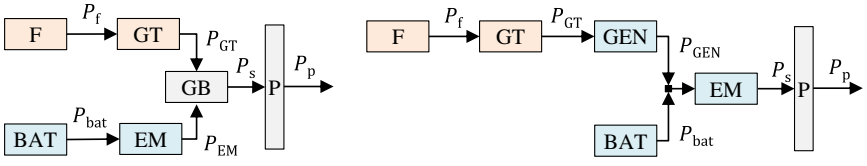

a) Parallel **b) Serial**

Fig. 2 Simplified representation of the parallel and serial powertrain architectures.

Table 2 Mission and performance requirements

Parameter	Value	Parameter	Value
Takeoff distance [m]	793	Diversion speed V_{div} [m/s]	85
Taxi/takeoff altitude h_{TO} [m]	0	AEO ROC at SL [m/s]	8
Cruise altitude h_{cr} [m]	3000	OEI ROC at SL [m/s]	2
Landing/taxi altitude h_L [m]	0	Range (baseline) R [km]	396
Diversion altitude h_{div} [m]	1000	Diversion range R_{div} [km]	270
Loiter altitude h_{loiter} [m]	450	Loiter time [min]	30
Cruise speed V_{cr} [m/s]	115	Contingency fuel [%]	5
Stall speed V_s [m/s]	34.5	Payload (baseline) m_{PL} [kg]	1960

on the Do 228 [48], but are designed to produce up to 701 kW [49]. The reference aircraft is sized for a typical commuter mission, including diversion, 30 minutes of loiter, and additional contingency fuel reserves, as specified by the regulations [51]. The mission specification and top-level design requirements are shown in Table 2.

The selected aircraft performance requirements are based on information given in Refs. [48,50], whereas the propulsion system data are obtained from manufacturer data and the Do 228 pilot's operating handbook [47]. The following deviation was made from the published data. The published takeoff distance is given as 793 m, including the climb to obstacle height. Using the pilot's operating handbook, takeoff ground roll is determined as 650 m. Moreover, the mission requirements are extracted from the payload-range diagram of the aircraft, presented in Fig. 3.

The values of the design parameters and additional input assumptions selected to meet these top-level requirements are included in the Appendix for traceability. The aerodynamic modeling is discussed in Sec. IV.B. The designs were found to be especially sensitive to the aerodynamic modeling of the aircraft and to the performance characteristics of the turboshaft engine. For the power lapse and specific fuel consumption (or thermal efficiency) of the engine, a surrogate model was built based on TPE331 performance data [49]. Because of the flat-rating of the TPE331 used on the Do 228, the engine was found to be able to produce maximum power at all combinations of flight speed and altitude considered in this study. The specific fuel consumption of the engine, meanwhile, is computed as a function of flight speed and altitude using the surrogate model, and additionally corrected for part-throttle, as mentioned in Sec. III.C.

B. Aerodynamic Modeling

Because no aerodynamic data for the Do 228NG is available in the public domain, the aerodynamic performance had to be estimated by the authors. To increase fidelity, the authors decided against a classical drag buildup to determine the drag polar. Instead, Reynolds-averaged Navier–Stokes (RANS) computational fluid dynamics (CFD) simulations were carried out to determine the drag polar of the aircraft. The reference geometry was created in OpenVSP using 3-view drawings of the Do 228NG. That geometry would have been required too if drag buildup methods had been employed. However, while drag buildup methods are specifically developed for conceptual design, they are not able to capture airframe aerodynamics with their full complexity. The Do 228 features under-the-wing engines, which contribute considerably to interference drag and also reduce the wing efficiency [52]. Additionally, it has a box-shaped fuselage with multiple kinks and significant upsweep, which complicates drag estimation. These issues were discussed by Götten et al. [53], who highlight that drag buildup models can give significantly wrong results when applied to nonstandard aircraft configurations.

The simulation was set up according to the recommendations outlined in Ref. [54]. The OpenVSP geometry was transferred to Siemens's simulation package STAR-CCM+ via the .STL standard. Then, the flowfield about the models was simulated using a steady-state RANS approach, using the SST k-ω (Menter) turbulence model. Further details on this methodology can be found in Ref. [55]. The RANS equations were solved using the assumptions of incompressible flow with a semi-implicit method for pressure linked equations (SIMPLE) approach. The bullet-shaped flowfield was divided into finite volumes using the unstructured Cartesian cut cell mesher with a dedicated prism mesh, which discretizes the boundary layer. Boundary-layer thickness was determined using Schlichting's methods [56], ensuring y^+ values below 1 on the aircraft surfaces. The surface mesh size was adjusted to give approximately 70 cells over the wing in chordwise direction. Lift and drag forces on the model bodies were obtained by integrating the cell shear stress tensor and their pressures. To decrease the computational effort, a half-model was used, and a symmetry condition was applied. Grid-independent results were then obtained for a mesh size of 18.5 million cells, as shown in Fig. 4. At this grid level, the grid-convergence error of L/D is less than 1%. The mesh optimization scheme of STAR–CCM+ was employed, which improves cell skewness angles, cell aspect ratio, and volume change between cells. Further information on the simulation parameters is presented in Table 3. A sample pressure coefficient distribution is shown in Fig. 5.

Nine operating points were calculated using this approach, ranging from −4 to 10° angle of attack, in steps of 2°. A curve fit was subsequently applied to find the lift coefficient at minimum drag, $C_{L,\min D}$, the minimum drag coefficient, $C_{D\min}$, and Oswald's aircraft efficiency factor e. These parameters allow the construction of an asymmetric parabolic drag polar given by

$$C_D = C_{D,\min} + k \cdot (C_L - C_{L,\min D})^2 \tag{5}$$

$$k = \frac{1}{\pi \cdot A \cdot e} \tag{6}$$

Additionally, a penalty was applied to the drag values obtained from RANS CFD because the drag from leakage and protuberance, cooling, propeller interaction, and other miscellaneous drag sources are not accounted for. A 20% increase of the total zero-lift drag is appropriate to account for the underprediction of these effects by CFD [24]. The resulting aerodynamic parameters are shown in

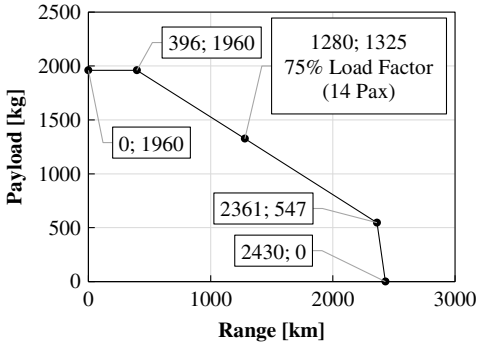

Fig. 3 Payload-range diagram of the Do 228NG. Data taken from Ref. [48].

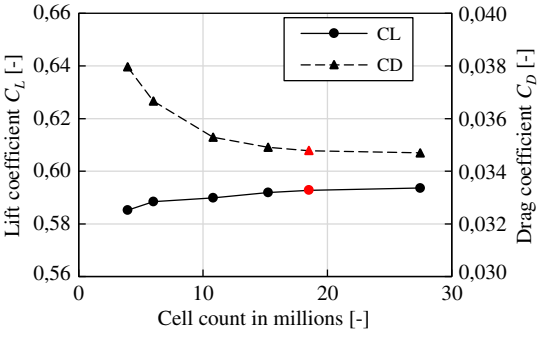

Fig. 4 Grid independence study, indicating the selected grid size in red ($\alpha = 2°$).

Table 3 Operating conditions selected for the CFD simulations of the reference aircraft geometry

Parameter	Value
Freestream velocity, V_∞ [m/s]	55
Reference pressure, p_∞ [Pa]	101,325
Density, ρ_∞ [kg/m^3]	1.225
Dynamic viscosity, μ [Pa · s]	$1.812 \cdot 10^{-5}$
Reynolds number, Re_{MGC}	$6.967 \cdot 10^6$
Mach number, M_∞	0.161
Turbulence intensity (inlet)	1%
Turbulent viscosity ratio (inlet)	10

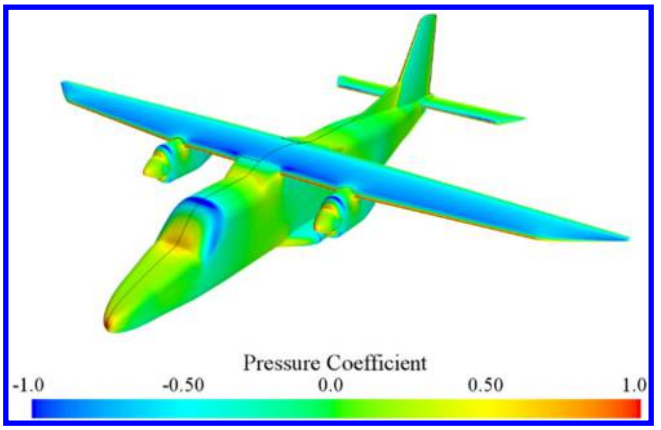

Fig. 5 Pressure coefficient distribution on the aircraft model at $\alpha = 0°$. Propeller effects not included.

Table 4. The lift and drag characteristics are presented in Fig. 6. A maximum L/D of 16 is obtained at a C_L of 0.75.

C. Sizing of the Reference Aircraft

The first step of the sizing process is to determine the wing loading and power-loading or power-to-weight ratio of the aircraft. To this end, the results obtained from both methods for the Do 228 are shown in Fig. 7. The constraint lines are constructed with the requirements from Sec. IV.A and the aerodynamic data from Sec. IV.B. For completeness, all additional performance requirements specified by the regulations [57,58] have been included in gray lines in Fig. 7. However, these additional constraints were found to not actively constrain the design space and are therefore not discussed in further detail.

Table 4 Drag polar characteristics

Parameter	Value
Aspect ratio, A	9.00
Minimum drag coefficient, $C_{D,\min}$	0.029
Minimum-drag lift coefficient, $C_{L,\min D}$	0.17
Oswald's aircraft efficiency factor, e	0.63

The agreement of both methods is good, although slight variations can be observed in the diagram. The most glaring disparity is the takeoff distance constraint. Method A uses Gudmundsson's approach, which correlates W_{TO}/S and P_s/W_{TO} in a nonlinear fashion. Method B uses Raymer's linear regression approach, which gives more optimistic values at high wing loading. The one-engine inoperative (OEI) rate-of-climb (ROC) constraint at sea level (SL) is found to differ slightly due to the different flight speed assumed in either method (see Table 1), with method B being slightly more conservative. The all-engines operating (AEO) ROC constraint and the stall speed constraint, which determine the design point, are found to show a good agreement between the two methods, as well as the cruise speed constraint. Consequently, the design points obtained from both methods are practically identical and differ less than 1% from the design point of the Do 228 for the selected design parameters, as shown in Table 5.

Using the P/W_{TO} and W_{TO}/S data from the constraint diagrams, the mission performance analysis is carried out to determine the energy requirements of the desired mission. This is conducted for three different points of the Do 228 payload-range diagram: a short-range mission with maximum payload, a medium-range mission with 75% load factor, and a long-range mission that corresponds to maximum fuel and minimum payload (see Fig. 3). As the Do 228 flies all missions with the same MTOM, the sizing methods should also return the same gross mass for each of the points.

The sizing results of all points of the payload-range diagram are shown in Table 6 for both methods. The difference in MTOM between the reference aircraft and the sizing results of the numerical methods is less than 4%. This is a remarkable result, especially when considering that these methods are intended for conceptual design work, and the fidelity of the modeling is relatively low. As a general trend, method A seems to overestimate MTOM (+0.5 to +3.8%), but no clear trend regarding the influence of the design range can be seen. Method B gets an excellent result (+0.3%) for the short mission, but slightly underpredicts MTOM for longer ranges (up to −3.3%). Furthermore, to verify that the MTOM estimation of the aircraft is correct and not an artifact of counteracting effects in the component mass estimation, the component masses of both methods for each mission are compared with reference data in Fig. 8. This figure shows that, apart from the fuel mass, both methods are capable of sizing the different components with reasonable accuracy.

Figure 8 shows that the largest discrepancy between the reference and the results of both methods is found for the fuel mass. Fuel mass is directly connected to the overall efficiency of the aircraft, and almost all modeling errors manifest themselves in an increase or decrease in fuel burn. The sensitivity of fuel burn to the aerodynamic characteristics of the aircraft and to the performance map of the turboshaft engine make the discrepancy hard to trace back to a specific assumption or modeling error. The largest relative difference is found

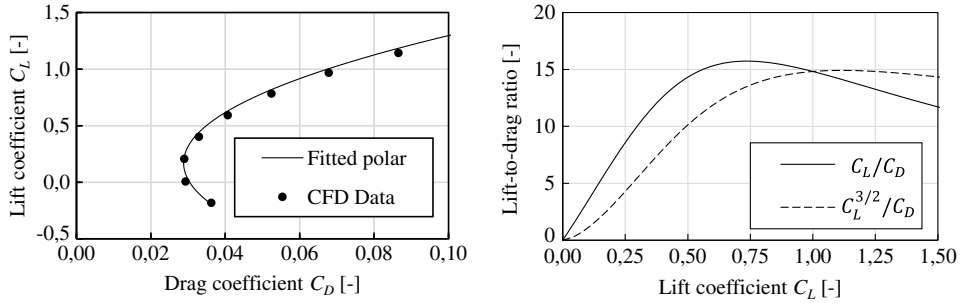

a) Drag polar **b) Lift-to-drag ratio**

Fig. 6 Drag polar characteristics obtained from the CFD simulations of the reference aircraft geometry.

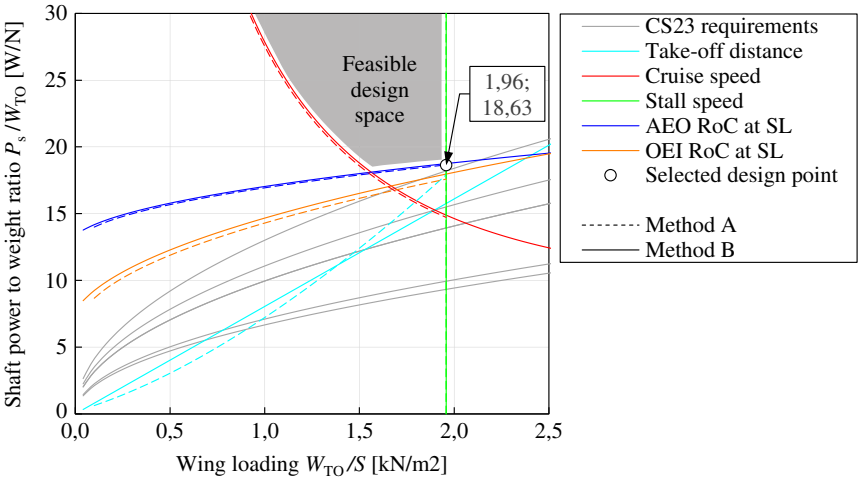

Fig. 7 Performance constraint diagram of the reference aircraft configuration, corrected to maximum throttle.

Table 5 Design point comparison

	Do 228	Method A		Method B	
Design point	Ref. data	Value	Diff., %	Value	Diff., %
W_{TO}/S [N/m^2]	1962	1957	−0.3	1958	−0.2
P_s/W_{TO} [W/N]	18.44	18.65	+1.1	18.63	+1.0

for the short-range mission, which also has the lowest absolute fuel mass. Consequently, the relative deviation from the reference data is the largest, even though the fuel mass is only overpredicted by approximately 60 kg (see Table A3). The larger error for shorter missions also suggests that different reserve-fuel requirements might play a role. For example, the diversion range of the reference aircraft might be lower than assumed here.

The inherent differences of the mission analyses of both methods play a factor as well: the taxi, takeoff, and landing fuel fractions are calculated differently; a different climb and descent strategy is used; the variable turboshaft efficiency is implemented differently, as discussed in Sec. III.C. Especially the last two points have an important effect for the shorter missions, as a larger fraction of the mission is spent in off-design conditions, instead of in cruise flight. To further investigate possible differences in the mission analysis, Fig. 9 shows the mission profile obtained by the two sizing methods for the short-range mission. Note that, for such a short mission, the reserves play an important role in determining the total fuel weight. Although no mission data are available for the reference aircraft, Fig. 9 shows that the two methods produce similar mission profiles. The climb and descent profiles of method B are smoother but lead to slightly higher energy consumption, as discussed in Sec. III.C. Moreover, method A explicitly models the taxi-out, takeoff, landing, and taxi-in phases, whereas method B does not. For method B, the nominal mission starts

Table 6 MTOM computed for the conventional aircraft configuration and comparison to reference aircraft data

Mission		Reference	Method A		Method B	
Range, km	Payload, t	MTOM, t	MTOM, t	Difference, %	MTOM, t	Difference, %
396	1.96	6.40	6.64	+3.8	6.42	+0.3
1280	1.33	6.40	6.43	+0.5	6.40	0.0
2361	0.55	6.40	6.49	+1.4	6.19	−3.3

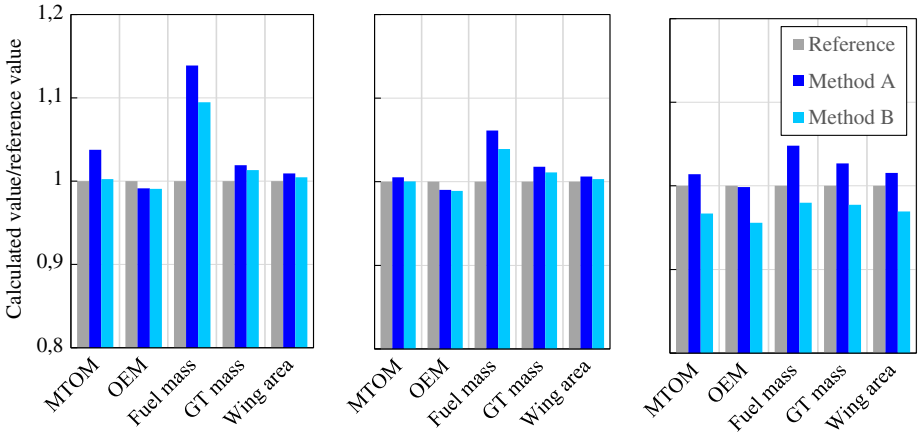

a) Short range mission **b) Medium range mission** **c) Long range mission**

Fig. 8 Comparison between results obtained from the two sizing methods and reference aircraft data.

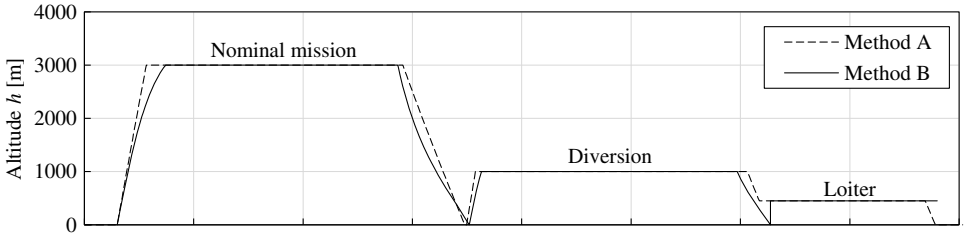

a) Altitude profile

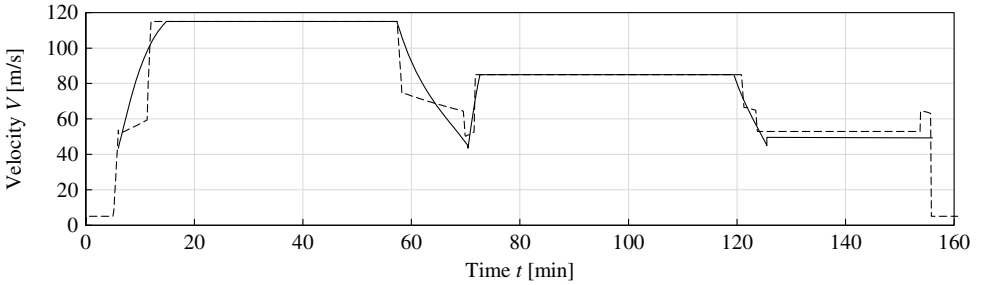

b) Velocity profile

Fig. 9 Reference aircraft altitude (top) and velocity (bottom) profiles for the short-range mission.

at takeoff speed and ends at the approach speed. Finally, method A always accelerates/decelerates and climbs/descends between mission phases, whereas method B presents a discontinuity at the beginning and end of the loiter phase, for which no transition phases are modeled. However, despite these differences, the block fuel consumption computed by the two methods does not differ significantly, as reflected in Fig. 8.

V. Hybrid-Electric Aircraft

In this section, the conventional, parallel-hybrid, serial-hybrid, and fully electric aircraft are compared against each other. The comparison is conducted in detail for the three missions that were analyzed in Sec. IV, and then, in more general terms, for three parameter sweeps.

A. Assumptions

The differences observed with the conventional baseline aircraft in Sec. IV can largely be attributed to different modeling approaches for the mission reserves and powertrain components. To exclude these differences—which are not inherent to the formulation of the two sizing methods—several additional simplifications are made for the comparison of hybrid-electric aircraft. In this way, the additional discrepancies due to the incorporation of hybrid-electric propulsion can be isolated. In the following paragraphs, the simplifications are briefly explained.

1. Turboprop Engines

For the comparison of (hybrid-) electric concepts, the thermal efficiency of the gas turbines is fixed, independently of the throttle setting or flight condition, and assumed to be $\eta_{GT} = 0.2112$. This corresponds to a BSFC of 398 $g/k \cdot Wh$, and is applied to both the (hybrid-) electric concepts and the conventional fuel-based reference aircraft, which is re-evaluated for this comparison. This value is obtained by calculating the average efficiency of the short-range mission, including the ground and diversion phases of the mission.

2. Electric Motors

The values of specific power and transmission efficiency assumed for the electrical machines (EM) and inverters/rectifiers are based on the state-of-the-art research goals presented in Ref. [59] and are gathered in Table 7. The EMs are assumed to achieve 13 kW/kg, and the specific power of the power converters is assumed to be 19 kW/kg. Because a thermal management system and additional elements of the power management and distribution (PMAD) system can significantly increase this system mass, the total mass of the electrical systems is increased by 30%. This generic mass penalty is assumed due to a lack of information in the preliminary sizing phase for an accurate estimation of the mass of components such as cooling systems or cables. Thus, the equivalent specific EM mass is assumed to be 5.92 kW/kg. To describe the losses of the entire electrical system, a constant equivalent motor efficiency of 95% is used, and all other component efficiencies are set to 100%.

3. Battery System

The battery system is modeled using a rudimentary "energy in a box" approach. Thus, an idealized constant potential battery is assumed. The internal resistance and other losses are assumed to be zero, and consequently, the efficiency of the battery is 100% (see Table 7). To preserve battery life and to account for energy reserves, a 20% state-of-charge margin is used. For the sake of comparison, futuristic technology assumptions are used, to allow for convergence of aircraft with high levels of hybridization and fully electric aircraft. With a specific energy $E^*_{bat} = 1500\ W \cdot h/kg$ and a $4C$ discharge rate, reasonable MTOM values could be achieved. The selection of more realistic, near-term battery technology would have resulted in many unconverged design points in the parameter sweeps. However, it is important to note that the technology values assumed for the batteries at pack level ($E^*_{bat} = 1500\ W \cdot h/kg$ and $P^*_{bat} = 6\ kW/kg$) must be considered beyond optimistic. The maximum theoretical specific energy of typical Li-Ion batteries (lithium cobalt oxide cells)

Table 7 Characteristics assumed for powertrain components

Parameter	Value
Turboshaft specific power, P^*_{GT} [kW/kg]	3.31
Turboshaft efficiency, η_{GT}	21.1%
Electrical machine specific power (equivalent), P^*_{EM}, P^*_{GEN} [kW/kg]	5.92
Electric machine efficiency (equivalent), η_{EM}, η_{GEN}	95%
Battery specific energy, E^*_{bat} [$W \cdot h/kg$]	1500
Battery specific power, P^*_{bat} [kW/kg]	6.0 ($= 4C$)
Battery efficiency, η_{bat}	100%
Minimum state-of-charge	20%

at cell level is 387 W · h/kg [60]. Lithium–sulfur or lithium–air batteries could reach specific energy levels over 2500 W · h/kg in theory but are far from being usable in practical, high-power applications [60].

4. *Mission Modeling*

For conventional 19-seater aircraft, a 5% contingency fuel reserve has to be maintained [51]. Given that for HEP aircraft it is unclear whether these energy reserves should be accounted for in the fuel energy, battery energy, or both, this 5% contribution to total energy is not included in the following analyses. Thus, the fuel mass is reduced compared with the conventional short-range results.

B. Comparison of Baseline Missions

In this section, the HEP variants are sized for the three reference missions presented in Sec III.A. Both methods differ in their approach to constructing the matching diagram, which is the first step of the sizing process. This is not only true with regard to the determination of the constraint lines, as discussed in Sec. IV, but also with respect to the determination of the power split of the components of the hybrid-electric powertrain. To illustrate the difference, Fig. 10 presents a series of matching diagrams obtained from method A and method B. For both methods, only the five driving constraints (as discussed in Sec. IV) are presented; other constraints from the certification specifications are neglected. As this example is only meant to further illustrate the different approaches of the methods, the matching diagrams are only shown for the parallel-hybrid propulsion architecture.

Method A attempts to simplify the matching process as much as possible. This allows using a graphical method to assess the hybrid electric design space. The results for any required figure of merit (e.g., MTOM, energy usage, or cost) can then be plotted and superimposed to the performance constraints. Such figures are

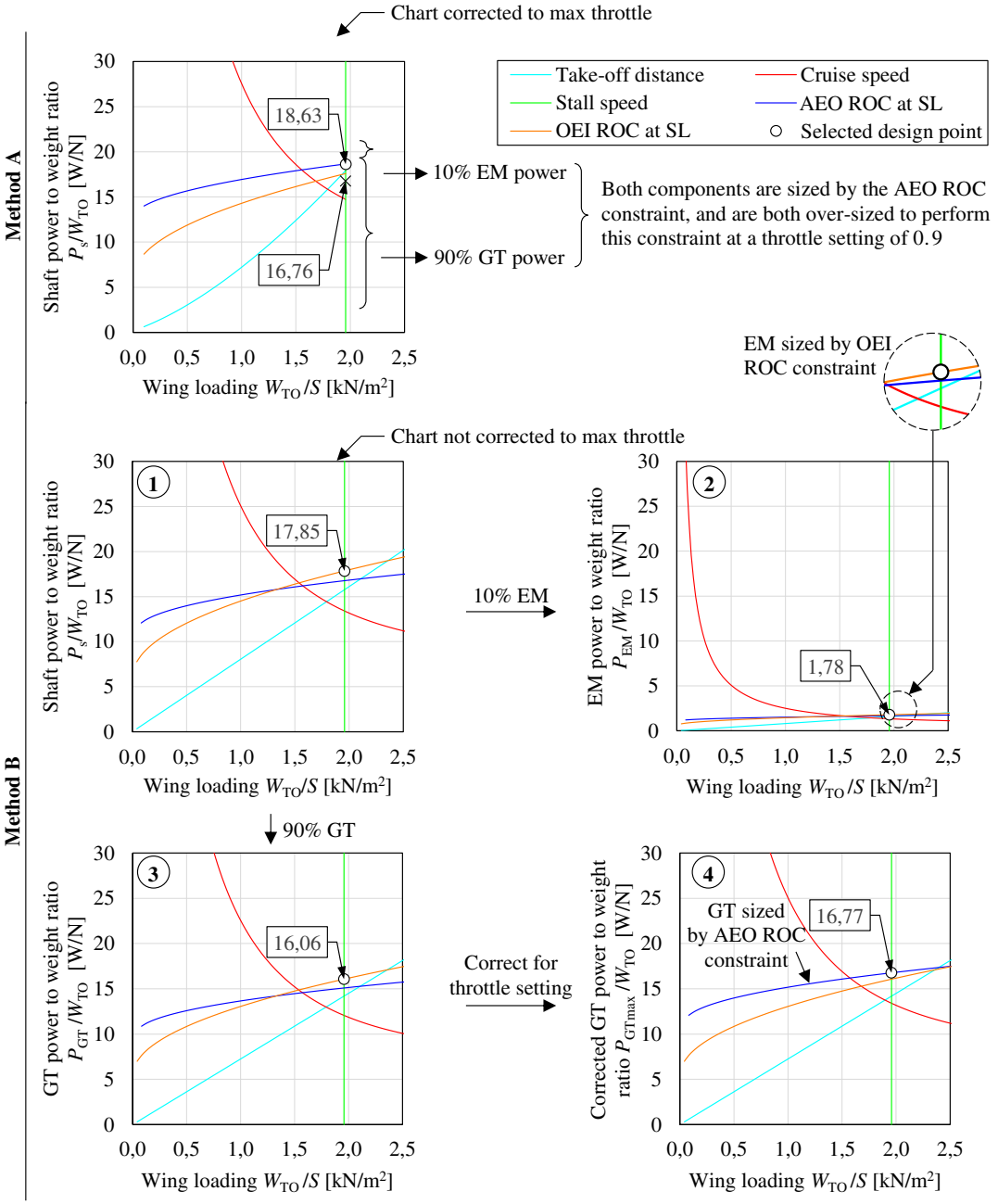

Fig. 10 Overview of how the constraint diagrams of method A (top) and method B (bottom) are used in the design process. Diagrams obtained for the parallel powertrain configuration.

sometimes called "thumbprint plots" and can be used to understand the hybrid-electric design space and select the best design point. More information can be found in Ref. [17]. However, finding a "best" design point is not the objective of this comparative study. Therefore, only a basic approach is explained: the constraint diagram is constructed, corrected to maximum throttle at sea level, as well as maximum takeoff mass, and subsequently, the design point is selected. In Fig. 10, the design point is 18.63 W/N at a wing loading of 1.96 kN/m^2. To find the power required for a predetermined hybridization ratio, the total power-to-weight ratio, P/W_{TO}, is split by the hybridization ratio. For the example in Fig. 10, a P/W_{TO} of 16.76 W/N is selected for the gas turbine, whereas the remaining difference between gas turbine power and total installed power is provided by the electric power system. In other words, a hybridization of 10% is used, and thus $P_{GT}/W_{TO} = 16.76$, and $P_{EM}/W_{TO} = 1.87$. Because the normalization to maximum gas-turbine throttle at sea level is applied to the total shaft power, the electric powertrain components are slightly oversized.

Method B, on the other hand, allows the designer to specify different power-control parameters (i.e., throttle and supplied power ratio) for each performance constraint. Hence, different components can be sized by different constraints, and none of the components is oversized. For example, if the batteries and electromotor were only used during climb, then they would be actively sized in that condition, whereas the gas turbine would have to provide only part power and would, therefore, be sized by a different constraint such as takeoff or cruise. However, compared with method A, this requires the designer to specify additional control settings, leading to a more complex interpretation of the matching diagrams, as evidenced in the bottom half of Fig. 10. This figure shows how first the shaft-power matching diagram is constructed (Fig. 10.B.1), based on which the matching diagrams of the remaining elements of the powertrain (see Fig. 2) are computed for a given power split. Because the power split is kept constant for all performance constraints in this study ($H_p = 0.1$), the relative positions of the constraints do not change much, although the power-to-weight ratio required from the electric motors is much lower than the gas turbine, as visible in Figs. 10.B.2 and 10.B.3. Given that different throttle settings are used for different constraints (see Table A2), the gas turbine has a different active constraint than the electric motors. Note that only the gas turbine is corrected for throttle setting, as shown in Fig. 10.B.4. Nevertheless, even though the two methods use fundamentally different approaches for the matching diagrams, the resulting design points are comparable. The gas-turbine power-to-weight ratio is virtually the same for both cases ($P_{GT}/W_{TO} = 16.76$ and 16.77 for methods A and B, respectively). The power-to-weight ratio obtained for the electrical motors is approximately 5% lower for method B ($P_{EM}/W_{TO} = 1.87$ and 1.78 for methods A and B, respectively) because it is not throttle-corrected.

Table 8 Maximum-take off mass values calculated for the conventional, parallel, serial, and fully electric powertrain configurations using the two sizing methods

Powertrain	Range, km	Payload, t	Method A MTOM, t	Method B MTOM, t	Difference, %
Conventional	396	1.96	6.22	6.26	+0.7
	1280	1.33	6.36	6.45	+1.3
	2361	0.55	7.08	7.18	+1.4
Parallel	396	1.96	6.36	6.39	+0.4
	1280	1.33	7.06	7.10	+0.6
	2361	0.55	13.47	13.36	−0.8
Serial	396	1.96	8.30	8.25	−0.6
	1280	1.33	12.52	12.35	−1.3
	2361	0.55	N/A	N/A	N/A
Electric	396	1.96	8.17	8.29	+1.5
	1280	1.33	N/A	N/A	N/A
	2361	0.55	N/A	N/A	N/A

N/A indicates that no converged design was obtained.

Using the P/W_{TO} and W_{TO}/S data from the constraint diagrams, the mission performance analysis is then carried out, and aircraft size is matched to the required mission performance. The resulting MTOM predicted by the two methods is presented in Table 8, including the difference of method B with respect to method A, which is calculated as $(MTOM_B - MTOM_A)/MTOM_A$. Additionally, the MTOM breakdown obtained for the short-range mission is shown in Fig. 11. In all cases, the differences between the two methods are well within the uncertainty of a class I sizing process. The most important conclusions that can be drawn are summarized in the following paragraphs.

1. *Conventional Powertrain*

The results for the conventional powertrain configuration (shown in Table 8) differ slightly from the results shown in Sec. IV, due to the simplified modeling approach taken for the HEP comparison. The discrepancy is larger for the short- and long-range missions than for the medium-range mission. For both methods, the MTOM obtained for the short-range mission is lower than in Sec. IV, because the average gas-turbine efficiency is accurate, but the fuel reserves are neglected. The MTOM obtained for the long-range mission, to the contrary, is overpredicted because, in this case, the exclusion of contingency fuel has a relatively lower impact, while the assumed gas-turbine efficiency is lower than in practice, due to the long cruise segment. Nevertheless, the agreement between both methods is good. The maximum difference in MTOM between method A and method B is less than 1.5%.

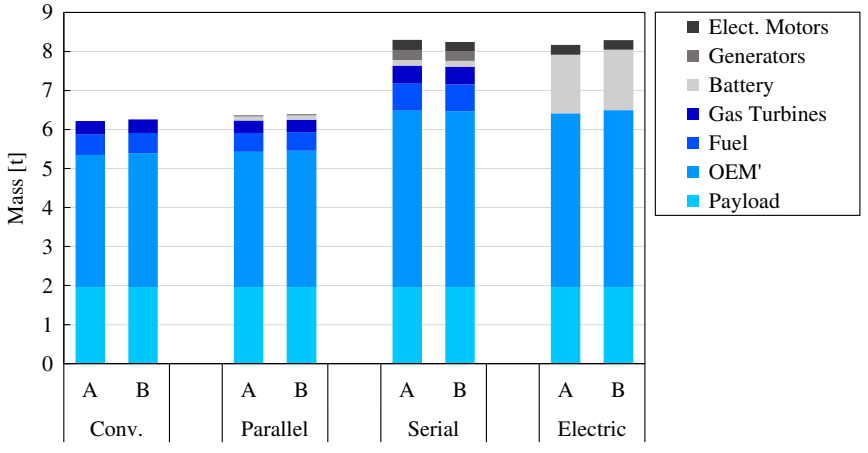

Fig. 11 Mass breakdown of the four powertrain configurations obtained using method A and method B, for the short-range mission ($R = 396$ km, $m_{PL} = 1.96$ t).

2. Parallel-Hybrid Powertrain

The results for the parallel hybrid powertrain show excellent agreement, with a difference of less than 1% between both methods. For both the parallel-hybrid and the serial-hybrid designs, the level of hybridization is fixed at 10%. For the parallel-hybrid, this means that the propeller is always supplied by 1 part electric motor power and 9 parts gas turbine power, joined through a gearbox with 100% efficiency. A converged design is obtained for all three missions, even though the long-range aircraft is more than twice as heavy as the short-range aircraft. Considering the very advanced technology assumptions that are made, this result indicates that efficient long-range flying with hybrid-electric propulsion systems is not a straightforward task. However, the detailed results for the short-range mission (Fig. 11) show that the fuel mass is reduced, when comparing against the conventional propulsion layout, even though MTOM increases.

3. Serial-Hybrid Powertrain

For this study, none of the prospective advantages (aeropropulsive interaction, distributed propulsion, etc.) of serial-hybrid designs are taken into account. The serial-hybrid powertrain is therefore expected to perform worse (heavier, less efficient) than the conventional or parallel-hybrid configurations. This is supported by the results presented in Table 8. Only the short- and medium-range mission have converged. For the long-range mission, the powertrain is too heavy and inefficient to converge—even with the highly optimistic technology assumptions. The results are very close (0.6% difference) for the short-range mission and still provide an acceptable agreement (1.6% difference) for the medium-range mission. It is worth noting that, just as for the parallel-hybrid powertrain, the level of hybridization is fixed at 10%. This means that the electric motor is always supplied by 1 part battery power and 9 parts generator power.

4. Fully Electric Powertrain

The final analysis is conducted for the fully electric powertrain configuration. Even with the highly optimistic technology assumptions, only the short-range mission converges for this powertrain architecture, as shown in Table 8. The medium- and long-range missions require an MTOM above 50 tons, which is infeasible for a 19-seat aircraft. Yet, both methods converged within 1.5% for the short-range mission. For this specific set of requirements and technology assumptions, the serial-hybrid short-range aircraft and the electric short-range aircraft converge to almost the same MTOM. In Fig. 11 it can be observed that the additional mass required by the batteries for the fully electric configuration completely compensates the weight reduction due to the absence of gas turbines, fuel, and generators. However, while method A predicts a higher MTOM than method B for the serial-hybrid short-range case, it predicts a lower MTOM for the electric short-range case. Therefore, no clear conclusion can be drawn regarding which of the two methods is more or less conservative.

C. Parameter Sweeps

As a final step of this validation study, the design methods are evaluated regarding their ability to properly account for changes in the technology level and TLARs. The reader is reminded that the aim is to compare the data and gradients obtained with the two methods, and not to study the impact of these parameters on the resulting aircraft design. In this process, the impact of three parameters is analyzed: range, battery specific energy, and the hybridization ratio. The baseline point for the parameter sweeps is the short-range mission. Thus, payload is fixed at 1.96 t, and the design range is fixed at 396 km. The baseline technology assumptions are the same as in Sec. V.B ($E^*_{\text{bat}} = 1500$ W · h/kg and $H_{\text{P}} = 0.1$). Mission range is swept between 100 and 2500 km, battery specific energy is swept between 100 and 2000 W · h/kg, and the hybridization ratio is varied between 0 and 1, all while maintaining the remaining parameters constant.

The results for the parameter sweeps are analyzed for two measures of merit: MTOM and PREE. MTOM is often used for comparison in aircraft design studies because it gives an indication of the "size" of the aircraft and has a direct impact on power requirements, energy requirements, production and maintenance costs, and the certification of the aircraft [23]. The payload-range energy efficiency (PREE) [42], meanwhile, is used as the figure of merit to evaluate the energy consumption of the aircraft. The PREE is defined as payload weight times the range of the aircraft, divided by the total energy consumed during the nominal mission (excluding reserves), i.e.,

$$\text{PREE} = \frac{W_{\text{PL}} \cdot R}{E_{\text{miss}}} \tag{7}$$

Therefore, this dimensionless parameter indicates how efficiently the aircraft can transport its payload over a determined distance during its day-to-day operation. In Eq. (7), the energy consumed during the nominal mission, E_{miss}, is calculated differently by the two methods:

$$E_{\text{miss,A}} = E_{\text{taxi out}} + E_{\text{TO}} + E_{\text{climb}} + E_{\text{cruise}} + E_{\text{descent}} \tag{8}$$

$$E_{\text{miss,B}} = E_{\text{taxi out}} + E_{\text{TO}} + E_{\text{climb}} + E_{\text{cruise}} + E_{\text{descent}} + E_{\text{landing}} + E_{\text{taxi in}} \tag{9}$$

While method B uses energy fractions that are known a priori for taxi, takeoff, and landing (see Table A5), method A specifically calculates the energy consumption in these phases. The landing phase and the taxi-in phase are analyzed after flying the diversion. Thus, these phases would be analyzed at a wrong mass. To avoid confusion, these phases were entirely disregarded for the calculation of E_{miss}. Thus, E_{miss} will be slightly lower for method A than for method B, resulting in higher PREE values. Nevertheless, the difference was confirmed to be minor.

The following subsections detail the three parameter sweeps separately. Data for these comparisons are provided in the Appendix so that these trade studies can be used as reference cases for benchmarking and validation of other design tools.

1. Range

The design range is varied from 100 to 2500 km. Thus, short-range missions of just 15 min flight time are covered at the low end, whereas the longest flight would last 6 h. Range is swept in steps of 100 km, and the results of the sweep are presented in Fig. 12.

Both plots—MTOM and PREE—correlate very well. All basic trends are captured. The MTOM plots show an exponential relationship for increasing ranges. When analyzing MTOM results, the conventional aircraft shows to be less sensitive to an increase in range, when compared with the other designs. The serial and parallel designs show a similar slope but present an offset. This can be attributed to the mass increase, which is inherent to the hybrid propulsion systems. The fully electric design shows the highest slope. This behavior is expected, due to the much lower specific energy of batteries, compared with fossil fuels.

PREE shows an almost linear relationship with range. Again, the highest sensitivity is observed for the fully electric aircraft, and the lowest sensitivity is observed for the conventional design. When results for methods A and B are compared, they show only subtle differences for PREE. Method A slightly overpredicts PREE compared with method B. This is expected because the energy summation is slightly different between the methods, as described previously. The difference is more pronounced at the lower ranges because the relative time spent for landing and taxi in is decreasing, as total flight time is increased.

If the CS-23 commuter mass limit of 8618 kg (19,000 lb) would be enforced, then the maximum range of the fully electric and serial hybrid designs would be limited to less than 450 km, while the conventional aircraft could achieve ranges of 1100 km, more than twice as far. However, even though the conventional aircraft is the lightest, its PREE is inferior to the electric and parallel hybrid design at ranges up to 1100 km. This shows the general trend that electric and hybrid-electric aircraft can be more efficient for short-distance

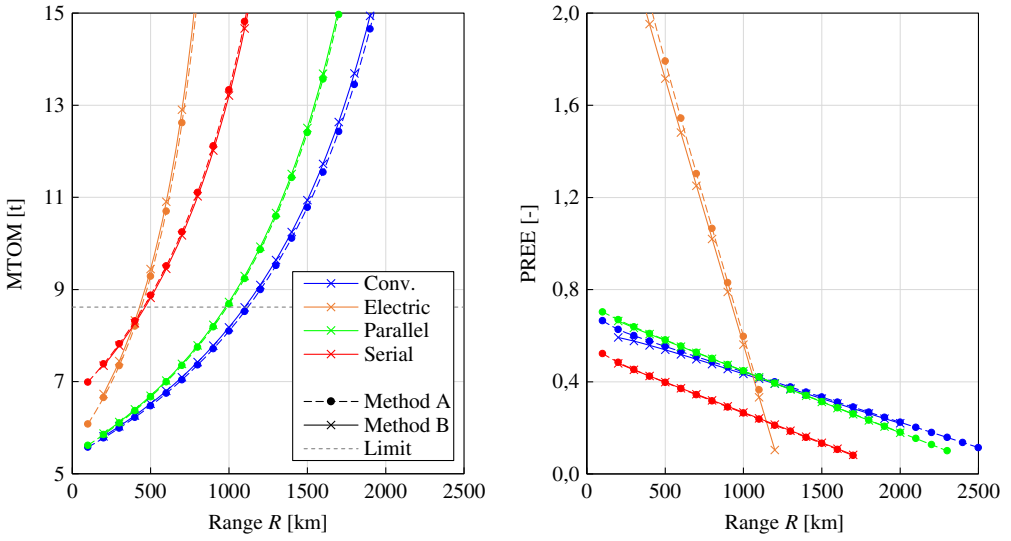

a) Maximum take-off mass **b) Payload-range energy efficiency**

Fig. 12 Maximum takeoff mass and PREE obtained for different mission ranges ($E^*_{\text{bat}} = 1500$ W · h/kg, $H_{\text{P}} = 0.1$). The gray dashed line indicates the MTOM limit for a 19-passenger commuter aircraft per CS-23 regulations.

flights, whereas longer ranges are most likely to be carried out by conventional aircraft. However, these are unoptimized designs with extremely optimistic technology assumptions, and thus no quantitative conclusions should be drawn from these data.

2. *Battery Technology Level*

The specific energy E^*_{bat} of the batteries is varied from 100 to 2000 W · h/kg. At the same time, the specific power P^*_{bat} is varied to maintain a constant discharge rate of 4C. Thus, $P^*_{\text{bat}} = 0.4$ kW/kg at 100 W · h/kg, while $P^*_{\text{bat}} = 8$ kW/kg at 2000 W · h/kg. E^*_{bat} is varied in steps of 100 W · h/kg, and the results of the sweep are presented in Fig. 13. For the 4C discharge rate limit assumed, the battery mass was found to be sized by energy requirements in all cases and not by power requirements. Thus, all missions are terminated with a 20% state-of-charge. It is worth noting that the extremely high specific energy levels of this study are far beyond the capabilities of practical batteries and are only used parametrically to show the corresponding sensitivities, as mentioned previously.

Again, the MTOM and PREE plots show very good correlation for all propulsion architectures. The expected trends are captured, with battery technology having no influence on conventional designs. For the remaining configurations, improving battery performance will yield lighter aircraft, which will be more efficient. Thus, for this study, PREE is roughly inversely proportional to MTOM. The absolute differences in MTOM between methods A and B are more pronounced at lower technology levels because the aircraft become heavier.

Method A again slightly overpredicts PREE when compared with method B. For this analysis, the relative error of the PREE calculation remains nearly constant across the sweep, because the mission range is not varied. The difference in PREE is more evident for the fully electric configuration (approximately 5% for the baseline $E^*_{\text{bat}} = 1500$ W · h/kg) and is also reflected in the MTOM comparison. This discrepancy is more prominent for the fully electric configuration due to the higher battery weight fraction and subsequent higher sensitivity to battery specific energy.

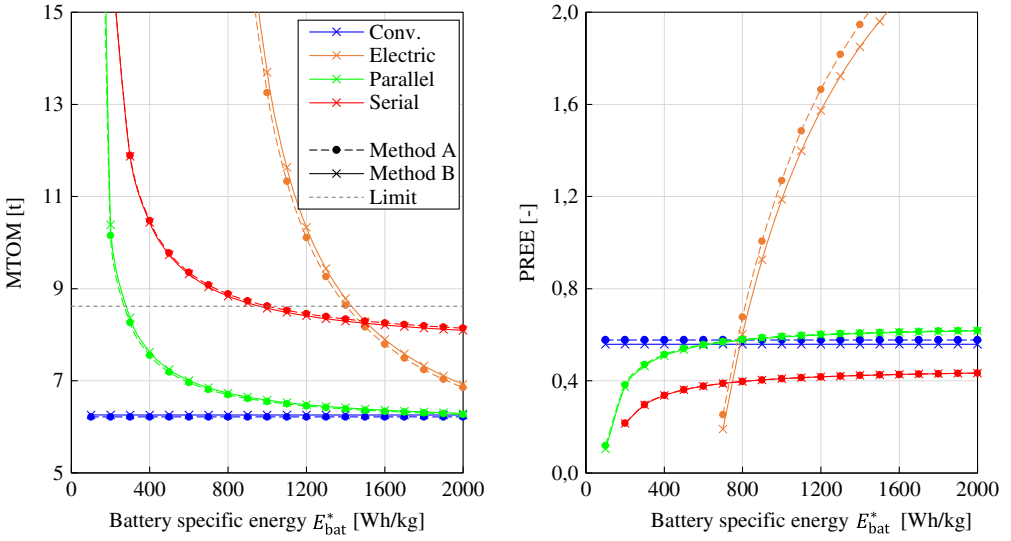

a) Maximum take-off mass **b) Payload-range energy efficiency**

Fig. 13 Maximum takeoff mass and PREE obtained for different battery technology levels ($R = 396$ km, $H_{\text{P}} = 0.1$). The gray dashed line indicates the MTOM limit for a 19-passenger commuter aircraft per CS-23 regulations.

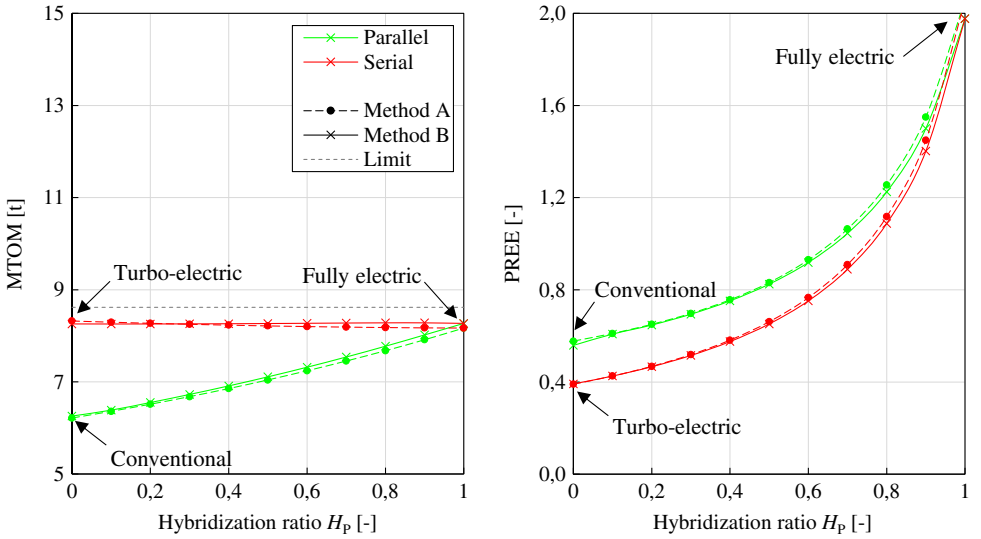

a) Maximum take-off mass **b) Payload-range energy efficiency**

Fig. 14 Maximum takeoff mass and PREE obtained for different hybridization ratios ($R = 396$ km, $E^*_{bat} = 1500$ W · h/kg). The gray dashed line indicates the MTOM limit for a 19-passenger commuter aircraft per CS-23 regulations.

Figure 13 shows that the CS-23 mass limit requires an E^*_{bat} of at least 1450 W · h/kg to allow for a fully electric design. This indicates that electric propulsion systems will not be a drop-in replacement for conventional propulsion systems in the near future, for the missions considered. However, a design with such kind of batteries would reach three times the PREE of the conventional aircraft. Benefits in terms of PREE can already be observed for batteries that exceed 800 W · h/kg. However, these aircraft would be four times heavier than comparable conventional aircraft, due to the snowball effect of the sizing process. Finally, Fig. 13 also shows that parallel architectures can present minor improvements in PREE if the battery specific energy is increased beyond 700 W · h/kg. Serial powertrains, on the other hand, are always outperformed by conventional fuel-based powertrains, because no hypothetical improvements in aeropropulsive efficiency or gas-turbine efficiency are included in this study.

3. *Hybridization Ratio*

The hybridization ratio of the propulsion system is varied from 0 to 100% in steps of 10%. Note that the hybridization ratio is defined differently for serial and parallel powertrains, as discussed in Sec. III.D. In both cases, a hybridization ratio of 100% corresponds to a fully electric aircraft, which exclusively uses batteries. However, for a serial architecture, a hybridization of 0% corresponds to a turbo-electric aircraft, whereas for a parallel architecture, the powertrain is reduced to a conventional fuel-based engine. Consequently, Fig. 14 shows the results of the parameter sweeps for the serial and parallel powertrains, whereas the conventional and fully electric configurations are obtained as limit cases of these two sweeps.

Once more, the MTOM and PREE plots show a very good correlation between the methods for both propulsion architectures. The parallel hybrid with a hybridization ratio of 0% corresponds to a conventional aircraft and is, therefore, the lightest solution for the given mission. As the hybridization ratio is increased, the weight fraction of the electric power systems of the aircraft increases. However, as MTOM increases, so does PREE. At 100% hybridization, the fully electric configuration is reached. The data points at $H_{P,PH} = 0.0$, 0.1, and 1.0 can also be found in the previous diagrams. The serial hybrid with a hybridization of 0% corresponds to a turbo-electric propulsion configuration that uses no buffer battery. As $H_{P,SH}$ increases, the gas turbine size is reduced, and batteries are added until the fully electric configuration is reached at $H_{P,SH} = 1.0$.

Figure 14a shows that, for the serial powertrain, MTOM is practically insensitive to the hybridization ratio, while PREE improves with increasing hybridization. The authors suspected that this almost constant relationship between H_P and MTOM is specific for this set of input parameters and not a trend inherent to the type of propulsion system in general. To confirm this hypothesis, the hybridization sweep of the serial hybrid architecture was also conducted for batteries with a specific energy of 3000 W · h/kg. The results are not shown here, but for that case, MTOM was found to vary significantly with the level of hybridization. Therefore, the lack of a gradient is a coincidence. For the selected input parameters, the increase in battery mass as H_P increases compensates the decrease in engine, generator, and fuel mass.

VI. Conclusions

This paper presents the cross-validation of two independently developed sizing methods. First, key aspects that need to be considered when validating sizing methods are discussed and the validation procedure outlined. Then, for the actual validation procedure, two independently developed preliminary sizing methods for hybrid-electric aircraft are compared in detail.

The design methods from FH Aachen and TU Delft are used to evaluate a 19-passenger commuter aircraft. The fuel-based reference aircraft is first sized for three points of the payload-range diagram. The results obtained from the two methods deviate from the reference data by approximately 1% in terms of power-to-weight ratio, and by less than 4% in terms of MTOM. The discrepancy in MTOM is predominantly attributed to uncertainties in component modeling and variations in the mission profile.

The two methods are then used to evaluate parallel, serial, and fully electric configurations. When comparing the different powertrain architectures for the three payload-range combinations selected, a difference in MTOM of less than 2% is observed between the two methods. Additionally, three parameter sweeps are performed, in order to analyze the sensitivity of MTOM and PREE to mission range, battery specific energy, and the hybridization ratio of the aircraft. The results of these sweeps show an excellent agreement in both slope and offset between the two methods. The largest deviations are observed for the fully electric configuration, due to the sensitivity of the battery-weight fraction to energy consumption. This leads to a PREE difference between the two methods of approximately 5% for the baseline mission requirements and technology assumptions.

These differences observed lie well within the uncertainty of the class I sizing process and confirm the correct implementation of the two methods. Although this does not necessarily guarantee that the formulation of the methods is flawless—because both methods might coincidentally be based on the same, inaccurate assumption—the agreement of results significantly increases the confidence in these two formulations. This is further evidenced by the trends observed in the parameters sweeps, which coincide with those expected from literature.

Moreover, throughout this study, the differences between the two methods are exposed as much as possible, such that the results can be used as a benchmark by the aircraft design community to compare and validate other design methods for hybrid-electric aircraft.

Appendix: Aircraft Sizing Data

Table A1 Additional design parameters and assumptions that are not included in Tables 2, 4, and 7

Parameter	Value	Parameter	Value
Number of propellers	2	Takeoff lift coefficient $C_{L,\mathrm{TO}}$[a]	1.34
PMAD efficiency, η_{PM}	1.0	$\Delta C_{L\,\max}$, takeoff flaps	0.73
Gearbox efficiency, η_{GB}	1.0	$\Delta C_{L\,\max}$, landing flaps	0.97
Fuel specific energy, E_{f}^{*} [MJ/kg][b,c]	42.8	$\Delta C_{D,\min}$, takeoff flaps[c]	0.010
Empty weight fraction, OEM/MTOM[c]	0.600	$\Delta C_{D,\min}$, landing flaps[c]	0.045
Empty weight fraction, OEM′/MTOM[a]	0.545	$\Delta C_{D,\min}$, landing gear[c]	0.015
Ambient density [kg/m^3]	ISA	$\Delta C_{L,\min D}$, takeoff flaps[c]	0
Ambient temperature [°C]	ISA	$\Delta C_{L,\min D}$, landing flaps[c]	0
Coefficient of rolling friction[a]	0.04	Δe, takeoff flaps[c]	0.040
Maximum lift coefficient (clean), $C_{L\,\max}$	1.70	Δe, landing flaps[c]	0.125

[a]Parameters only required for method A.
[b]Note that BSFC $= 1/(\eta_{\mathrm{GT}} E_{\mathrm{f}}^{*})$.
[c]Parameters only required for method B.

Table A2 Assumed aircraft properties per performance constraint and mission segment

		Throttle	Velocity, m/s	Mass fraction m/m_{TO}	Propulsive efficiency	Flap setting	Landing gear position
Constraints	Cruise	0.9	115	1	0.8	Retracted	Retracted
	Takeoff	1	—[a]/$1.2V_{\mathrm{s}}$[b,c]	1	0.7	Takeoff	Extended
	Landing	0.9	34.6	1	0.8	Landing	Extended
	AEO ROC	0.9	$V_{\text{best climb}}$[a]/$1.2V_{\mathrm{s}}$[b,c]	1	0.7	Retracted	Retracted
	OEI ROC	1	$V_{\text{best climb}}$[a]/$1.2V_{\mathrm{s}}$[b,c]	1	0.65	Retracted	Retracted
Mission analysis	Climb	0.9	— —	— —	0.8	Retracted	Retracted
	Cruise	— —	115	— —	0.8	Retracted	Retracted
	Descent	0,10[a]/0,05[b]	— —	— —	0.8	Retracted	Retracted
	Div. climb	0.9	— —	— —	0.8	Retracted	Retracted
	Div. cruise	— —	82	— —	0.8	Retracted	Retracted
	Div. descent	0,10[a]/0,05[b]	— —	— —	0.8	Retracted	Retracted
	Loiter	— —	53[a]/$V_{\text{max endurance}}$[b]	— —	0.8	Retracted	Retracted

A dash (—) indicates that the quantity is not an input, but a computed value.
[a]Values used for method A.
[b]Values used for method B.
[c]Stall speed in the flight condition considered.

Table A3 Component masses and wing area obtained in the reference aircraft comparison

Mission	Method	MTOM, kg	OEM, kg	m_{PL}, kg	m_f, kg	m_{GT}, kg	S, m^2
396 km	Reference	6400	3900	1960	540	349	32.0
	A	6641	3866	1960	615	356	32.3
	B	6416	3865	1960	591	354	32.2
1280 km	Reference	6400	3900	1325	1175	349	32.0
	A	6434	3862	1325	1247	356	32.2
	B	6403	3857	1325	1221	353	32.1
2361 km	Reference	6400	3900	547	1953	349	32.0
	A	6489	3895	547	2047	359	32.5
	B	6188	3728	547	1914	341	31.0

Table A4 Component masses and wing area obtained for the four different powertrain configurations in the HEP comparison study

Config.	Mission	Method	MTOM, kg	OEM, kg	m_{PL}, kg	m_f, kg	m_{bat}, kg	m_{GT}, kg	m_{GEN}, kg	m_{EM}, kg	S, m^2
Conv.	396 km	A	6,216	3,731	1,960	525	0	343	0	0.0	31.1
		B	6,259	3,770	1,960	529	0	345	0	0.0	31.4
	1280 km	A	6,364	3,820	1,325	1,219	0	352	0	0.0	31.9
		B	6,446	3,883	1,325	1,238	0	356	0	0.0	32.3
	2361 km	A	7,083	4,252	547	2,285	0	391	0	0.0	35.5
		B	7,182	4,325	547	2,310	0	396	0	0.0	36.0
Parallel	396 km	A	6,361	3,803	1,960	486	113	316	0	19.7	31.9
		B	6,385	3,830	1,960	481	115	317	0	18.9	32.0
	1280 km	A	7,058	4,219	1,325	1,222	292	351	0	21.8	35.4
		B	7,102	4,259	1,325	1,222	296	352	0	21.0	35.6
	2361 km	A	13,472	8,054	547	3,924	947	670	0	41.6	67.5
		B	13,363	8,014	547	3,863	939	663	0	39.5	66.9
Serial	396 km	A	8,295	5,490	1,960	697	148	457	256	256	41.6
		B	8,246	5,452	1,960	686	148	453	243	244	41.3
	1280 km	A	12,518	8,284	1,325	2,389	519	690	386	387	62.7
		B	12,354	8,168	1,325	2,348	513	679	364	365	61.9
	2361 km	A	N/A	N/A	N/A	N/A	N/A	N/A	N/A	N/A	N/A
		B	N/A	N/A	N/A	N/A	N/A	N/A	N/A	N/A	N/A
Electric	396 km	A	8,168	4,704	1,960	0	1504	0	0	252	40.9
		B	8,294	4,784	1,960	0	1550	0	0	245	41.6
	1280 km	A	N/A	N/A	N/A	N/A	N/A	N/A	N/A	N/A	N/A
		B	N/A	N/A	N/A	N/A	N/A	N/A	N/A	N/A	N/A
	2361 km	A	N/A	N/A	N/A	N/A	N/A	N/A	N/A	N/A	N/A
		B	N/A	N/A	N/A	N/A	N/A	N/A	N/A	N/A	N/A

N/A indicates that no converged design was obtained.

Table A5 Taxi, takeoff, and landing energy fractions assumed for method B, based on the estimations of method A, for the three missions considered

		Short range	Medium range	Long range
Configuration	Mission phase	$R = 396$ km, $m_{PL} = 1960$ kg	$R = 1280$ km, $m_{PL} = 1325$ kg	$R = 2361$ km, $m_{PL} = 547$ kg
Conventional	Taxi out & takeoff	2.6%	1.3%	0.8%
	Landing & taxi in	1.6%	0.8%	0.5%
Parallel	Taxi out & takeoff	2.1%	0.9%	0.6%
	Landing & taxi in	0.7%	0.3%	0.2%
Serial	Taxi out & takeoff	2.2%	0.9%	N/A
	Landing & taxi in	0.7%	0.3%	N/A
Electric	Taxi out & takeoff	1.6%	N/A	N/A
	Landing & taxi in	0.1%	N/A	N/A

Energy fractions expressed as a percentage of total installed energy (including reserves). *N/A* indicates that no converged design was obtained.

Table A6 Hybridization-ratio sweep results obtained from methods A and B ($m_{PL} = 1960$ kg, $R = 396$ km, $E^*_{bat} = 1500$ W · h/kg)

	Parallel				Serial			
	MTOM, kg		PREE		MTOM, kg		PREE	
H_p	A	B	A	B	A	B	A	B
0.0	6216	6258	0.577	0.559	8321	8258	0.390	0.392
0.1	6361	6386	0.611	0.608	8295	8256	0.426	0.426
0.2	6515	6552	0.650	0.647	8271	8257	0.468	0.466
0.3	6679	6727	0.698	0.694	8250	8259	0.519	0.515
0.4	6855	6912	0.757	0.752	8231	8262	0.582	0.575
0.5	7042	7109	0.832	0.825	8214	8266	0.661	0.652
0.6	7241	7318	0.930	0.919	8200	8272	0.766	0.752
0.7	7452	7540	1.064	1.045	8188	8277	0.909	0.889
0.8	7676	7774	1.255	1.225	8179	8281	1.118	1.087
0.9	7914	8019	1.549	1.500	8172	8281	1.449	1.402
1.0	8168	8269	2.060	1.976	8168	8269	2.060	1.976

Table A7 Range sweep results obtained from methods A and B ($m_{PL} = 1960$ kg, $E^*_{bat} = 1500$ W · h/kg, $H_P = 0.1$)

	Conventional				Parallel				Serial				Electric			
	MTOM, kg		PREE		MTOM, kg		PREE		MTOM, kg		PREE		MTOM, kg		PREE	
Range [km]	A	B	A	B	A	B	A	B	A	B	A	B	A	B	A	B
100	5,576	N/A	0.665	N/A	5,619	N/A	0.703	N/A	6,991	N/A	0.522	N/A	6,080	N/A	2.281	N/A
200	5,777	5,812	0.627	0.592	5,850	5,871	0.669	0.664	7,384	7,348	0.484	0.480	6,654	6,733	2.666	2.461
300	5,993	6,030	0.600	0.577	6,100	6,122	0.638	0.634	7,823	7,781	0.453	0.452	7,349	7,445	2.329	2.197
400	6,225	6,267	0.576	0.558	6,372	6,397	0.610	0.607	8,316	8,269	0.425	0.425	8,206	8,327	2.049	1.952
500	6,476	6,521	0.553	0.539	6,669	6,696	0.582	0.580	8,875	8,821	0.397	0.398	9,289	9,443	1.792	1.715
600	6,747	6,798	0.531	0.518	6,994	7,025	0.555	0.553	9,513	9,451	0.370	0.372	10,701	10,907	1.545	1.482
700	7,041	7,098	0.509	0.498	7,353	7,386	0.528	0.526	10,249	10,177	0.344	0.346	12,620	12,905	1.303	1.251
800	7,362	7,426	0.487	0.477	7,749	7,786	0.501	0.499	11,106	11,021	0.317	0.320	15,377	15,801	1.066	1.020
900	7,713	7,785	0.465	0.456	8,190	8,231	0.474	0.473	12,119	12,019	0.291	0.293	19,675	20,372	0.831	0.790
1,000	8,099	8,179	0.443	0.434	8,683	8,730	0.447	0.446	13,333	13,211	0.264	0.267	27,309	28,669	0.597	0.561
1,100	8,524	8,615	0.421	0.413	9,239	9,293	0.421	0.419	14,816	14,665	0.238	0.241	44,623	48,357	0.365	0.333
1,200	8,996	9,100	0.399	0.392	9,870	9,931	0.394	0.393	16,668	16,475	0.212	0.214	N/A	N/A	N/A	N/A
1,300	9,523	9,641	0.377	0.370	10,594	10,663	0.367	0.366	19,045	18,793	0.185	0.188	N/A	N/A	N/A	N/A
1,400	10,115	10,250	0.355	0.349	11,430	11,511	0.341	0.339	22,209	21,867	0.159	0.162	N/A	N/A	N/A	N/A
1,500	10,785	10,939	0.334	0.327	12,408	12,505	0.314	0.313	26,627	26,132	0.133	0.135	N/A	N/A	N/A	N/A
1,600	11,548	11,726	0.312	0.305	13,569	13,684	0.287	0.286	33,234	32,456	0.106	0.109	N/A	N/A	N/A	N/A
1,700	12,428	12,634	0.290	0.284	14,968	15,106	0.261	0.259	44,187	42,808	0.080	0.083	N/A	N/A	N/A	N/A
1,800	13,451	13,691	0.268	0.262	16,686	16,857	0.234	0.232	N/A	N/A	N/A	N/A	N/A	N/A	N/A	N/A
1,900	14,657	14,940	0.246	0.241	18,848	19,064	0.207	0.206	N/A	N/A	N/A	N/A	N/A	N/A	N/A	N/A
2,000	16,099	16,407	0.224	0.220	21,651	21,932	0.180	0.179	N/A	N/A	N/A	N/A	N/A	N/A	N/A	N/A
2,100	17,854	18,270	0.202	0.197	25,431	25,808	0.154	0.152	N/A	N/A	N/A	N/A	N/A	N/A	N/A	N/A
2,200	20,039	20,558	0.180	0.175	30,804	31,356	0.127	0.125	N/A	N/A	N/A	N/A	N/A	N/A	N/A	N/A
2,300	22,830	23,491	0.158	0.154	39,050	39,912	0.100	0.098	N/A	N/A	N/A	N/A	N/A	N/A	N/A	N/A
2,400	26,522	27,405	0.136	0.132	N/A	54,876	N/A	0.072	N/A	N/A	N/A	N/A	N/A	N/A	N/A	N/A
2,500	31,637	32,871	0.114	0.110	N/A	87,721	N/A	0.045	N/A	N/A	N/A	N/A	N/A	N/A	N/A	N/A

N/A indicates that no converged design was obtained.

Table A8 Battery specific-energy sweep results obtained from methods A and B ($m_{PL} = 1960$ kg, $R = 396$ km, $H_P = 0.1$)

	Conventional				Parallel				Serial				Electric			
	MTOM, kg		PREE		MTOM, kg		PREE		MTOM, kg		PREE		MTOM, kg		PREE	
E^*_{bat}, Wh/kg	A	B	A	B	A	B	A	B	A	B	A	B	A	B	A	B
100	6,216	6,259	0.577	0.559	32,546	37,160	0.119	0.104	N/A	N/A	N/A	N/A	N/A	N/A	N/A	N/A
200	6,216	6,257	0.577	0.559	10,153	10,385	0.383	0.374	16,321	16,352	0.216	0.215	N/A	N/A	N/A	N/A
300	6,216	6,257	0.577	0.559	8,259	8,365	0.470	0.464	11,895	11,868	0.297	0.296	N/A	N/A	N/A	N/A
400	6,216	6,257	0.577	0.559	7,555	7,626	0.514	0.509	10,474	10,437	0.337	0.337	N/A	N/A	N/A	N/A
500	6,216	6,257	0.577	0.559	7,187	7,243	0.541	0.536	9,774	9,733	0.361	0.361	N/A	N/A	N/A	N/A
600	6,216	6,257	0.577	0.559	6,961	7,007	0.558	0.554	9,357	9,314	0.377	0.377	N/A	N/A	N/A	N/A
700	6,216	6,257	0.577	0.559	6,808	6,848	0.571	0.567	9,080	9,036	0.389	0.389	66,422	85,005	0.253	0.191
800	6,216	6,257	0.577	0.559	6,697	6,734	0.580	0.576	8,883	8,838	0.398	0.397	24,862	26,951	0.677	0.603
900	6,216	6,257	0.577	0.559	6,614	6,647	0.587	0.584	8,736	8,690	0.404	0.404	16,724	17,551	1.006	0.925
1,000	6,216	6,257	0.577	0.559	6,549	6,580	0.593	0.590	8,621	8,576	0.410	0.410	13,253	13,698	1.270	1.186
1,100	6,216	6,257	0.577	0.559	6,496	6,526	0.598	0.595	8,530	8,484	0.414	0.414	11,329	11,628	1.485	1.398
1,200	6,216	6,257	0.577	0.559	6,453	6,481	0.602	0.599	8,455	8,409	0.418	0.418	10,107	10,329	1.665	1.573
1,300	6,216	6,257	0.577	0.559	6,417	6,444	0.605	0.602	8,393	8,347	0.421	0.421	9,261	9,436	1.817	1.722
1,400	6,216	6,257	0.577	0.559	6,387	6,413	0.608	0.605	8,340	8,294	0.423	0.423	8,642	8,784	1.947	1.850
1,500	6,216	6,257	0.577	0.559	6,361	6,386	0.611	0.608	8,295	8,249	0.426	0.426	8,168	8,289	2.060	1.960
1,600	6,216	6,257	0.577	0.559	6,338	6,362	0.613	0.610	8,256	8,209	0.428	0.428	7,794	7,899	2.159	2.057
1,700	6,216	6,257	0.577	0.559	6,318	6,341	0.615	0.612	8,222	8,175	0.430	0.430	7,492	7,584	2.246	2.143
1,800	6,216	6,257	0.577	0.559	6,300	6,323	0.617	0.614	8,192	8,145	0.431	0.431	7,242	7,324	2.323	2.218
1,900	6,216	6,257	0.577	0.559	6,285	6,307	0.618	0.616	8,165	8,118	0.433	0.433	7,032	7,107	2.393	2.286
2,000	6,216	6,257	0.577	0.559	6,271	6,292	0.620	0.617	8,141	8,094	0.434	0.434	6,853	6,922	2.455	2.348

N/A indicates that no converged design was obtained.

Acknowledgments

The authors would like to thank Maurice Hoogreef for helping with the evaluation of CS-23 requirements. The authors also thank Falk Götten, who provided valuable guidance on the setup of the CFD simulation. Finally, the authors like to express their gratitude to Siemens PLM Software for providing academic licenses of their software STAR-CCM+.

References

[1] De Breucker, S., Peeters, E., and Driesen, J., "Possible Applications of Plug-In Hybrid Electric Ships," *2009 IEEE Electric Ship Technologies Symposium*, April 2009. https://doi.org/10.1109/ESTS.2009.4906530

[2] Wilberforce, T., El-Hassan, Z., Khatib, F. N., Al Makky, A., Baroutaji, A., Carton, J. G., and Olabi, A. G., "Developments of Electric Cars and Fuel Cell Hydrogen Electric Cars," *International Journal of Hydrogen Energy*, Vol. 40, No. 40, Oct. 2017, pp. 25,695–25,734. https://doi.org/10.1016/j.ijhydene.2017.07.054

[3] Hepperle, M., "Electric Flight—Potential and Limitations," *AVT-209 Workshop*, 2012.

[4] Warwick, G., "Electric Potential—Are Battery Technologies Advancing Fast Enough to Enable eVTOL," Aviation Week & Space Technology, 14 Aug. 2017, pp. 38–41.

[5] Brelje, B. J., and Martins, J. R. R. A., "Electric, Hybrid, and Turboelectric Fixed-Wing Aircraft: A Review of Concepts, Models, and

Design Approaches," *Progress in Aerospace Sciences*, Vol. 104, 2018, pp. 1–0.
https://doi.org/10.1016/j.paerosci.2018.06.004

[6] Moore, M. D., and Fredericks, B., "Misconceptions of Electric Propulsion Aircraft and their Emergent Aviation Markets," *52nd Aerospace Sciences Meeting*, AIAA Paper 2014-0535, Jan. 2014.
https://doi.org/10.2514/6.2014-0535

[7] Juretzko, P. G., Immer, M., and Wildi, J., "Performance Analysis of a Hybrid Electric Retrofit of a RUAG Dornier Do 228NG," *CEAS Aeronautical Journal*, Vol. 11, Sept. 2019, pp. 263–275.
https://doi.org/10.1007/s13272-019-00420-2

[8] Wroblewski, G. E., and Ansell, P. J., "Mission Analysis and Emissions for Conventional and Hybrid-Electric Commercial Transport Aicraft," *Journal of Aircraft*, Vol. 56, No. 3, 2019, pp. 1200–1213.
https://doi.org/10.2514/1.C035070

[9] Moore, K. R., and Ning, A. N., "Takeoff and Performance Trade-Offs of Retrofit Distributed Electric Propulsion for Urban Transport," *Journal of Aircraft*, Vol. 56, No. 5, 2019, pp. 1880–1892.
https://doi.org/10.2514/1.C035321

[10] Glassock, R., Galea, M., Williams, W., and Glesk, T., "Hybrid Electric Aircraft Propulsion Case Study for Skydiving Mission," *Aerospace*, Vol. 4, No. 3, 2017, p. 45.
https://doi.org/10.3390/aerospace4030045

[11] Gnadt, A. R., Speth, R. L., Sabnis, J. S., and Barrett, S. R. H., "Technical and Environmental Assessment of All-Electric 180-Passenger Commercial Aircraft," *Progress in Aerospace Sciences*, Vol. 105, 2019, pp. 1–30.
https://doi.org/10.1016/j.paerosci.2018.11.002

[12] Voskuijl, M., Bogaert, J., and Rao, A. G., "Analysis and Design of Hybrid Electric Regional Turboprop Aircraft," *CEAS Aeronautical Journal*, Vol. 9, 2018, pp. 15–25.
https://doi.org/10.1007/s13272-017-0272-1

[13] Isikveren, A. T., Pornet, C., Vratny, P. C., and Schmidt, M., "Optimization of Commercial Aircraft Using Battery-Based Voltaic-Joule/Brayton Propulsion," *Journal of Aicraft*, Vol. 54, No. 1, 2019, pp. 246–261.
https://doi.org/10.2514/1.C033885

[14] Bijewitz, J., Seitz, A., Hornung, M., and Isikveren, A. T., "Progress in Optimizing the Propulsive Fuselage Aircraft Concept," *Journal of Aircraft*, Vol. 54, No. 5, 2017, pp. 1979–1989.
https://doi.org/10.2514/1.C034002

[15] Friedrich, C., and Robertson, P. A., "Hybrid-Electric Propulsion for Aircraft," *Journal of Aircraft*, Vol. 52, No. 1, Feb. 2015, pp. 176–189.
https://doi.org/10.2514/1.C032660

[16] de Vries, R., Hoogreef, M. F. M., and Vos, R., "Aeropropulsive Efficiency Requirements for Turboelectric Transport Aircraft," *AIAA Scitech 2020 Forum*, AIAA Paper 2020-0502, Jan. 2020.
https://doi.org/10.2514/6.2020-0502

[17] Finger, D. F., Braun, C., and Bil, C., "Initial Sizing Methodology for Hybrid-Electric General Aviation Aircraft," *Journal of Aircraft*, Vol. 57, No. 2, 2019, pp. 245–255.
https://doi.org/10.2514/1.C035428

[18] de Vries, R., Brown, M. T. H., and Vos, R., "Preliminary Sizing Method for Hybrid-Electric Distributed-Propulsion Aircraft," *Journal of Aircraft*, Vol. 56, No. 6, 2019, pp. 2172–2188.
https://doi.org/10.2514/1.C035388

[19] Basgall, B., Liu, W., Cassady, T., and Anemaat, W. A., "Aircraft Design Weight Methods Comparison and Improvement," *AIAA Scitech 2020 Forum*, AIAA Paper 2020-1259, Jan. 2020.
https://doi.org/10.2514/6.2020-1259

[20] Götten, F., Finger, D. F., Havermann, M., Braun, C., Marino, M., and Bil, C., "Full Configuration Drag Estimation of Small-to-Medium Range UAVs and its Impact on Initial Sizing Optimization," *CEAS Aeronautical Journal*, Vol. 12, 2021, pp. 589–603.
https://doi.org/10.1007/s13272-021-00522-w

[21] Götten, F., Havermann, M., Braun, C., Marino, M., and Bil, C., "Wind-tunnel and CFD Investigations of UAV Landing Gears and Turrets—Improvements in Empirical Drag Estimation," *Aerospace Science and Technology*, Vol. 107, Dec. 2020, pp. 1–15.
https://doi.org/10.1016/j.ast.2020.106306

[22] Raymer, D. P., *Aircraft Design: A Conceptual Approach*, 6th ed., AIAA, Reston, VA, 2018.
https://doi.org/10.2514/4.104909

[23] Nicolai, L. M., and Carichner, G. E., *Fundamentals of Aircraft and Airship Design—Volume I—Aircraft Design*, AIAA, Reston, VA, 2010.
https://doi.org/10.2514/4.867538

[24] Obert, E., *Aerodynamic Design of Transport Aircraft*, IOS Press, Amsterdam, 2009.

[25] Gudmundsson, S., *General Aviation Aircraft Design: Applied Methods and Procedures*, Butterworth-Heinemann, Oxford, 2014.

[26] Mattingly, J. D., Heiser, W. H., and Pratt, D. T., *Aircraft Engine Design*, 3rd ed., AIAA, Reston, VA, 2018.
https://doi.org/10.2514/4.105173

[27] Roskam, J., *Airplane Design Part I-VIII*, Roskam Aviation and Engineering Corp., Ottawa, KS, 1985.

[28] Loftin, L. K., Jr., *Subsonic Aircraft: Evolution and the Matching of Size to Performance*, NASA Langley, Langley, VA, 1980.

[29] Torenbeek, E., *Synthesis of Subsonic Airplane Design*, Delft Univ. Press, Delft, The Netherlands, 1982.

[30] Rings, R., Ludowicy, J., Finger, D. F., and Braun, C., "Sizing Studies of Light Aircraft with Parallel Hybrid Propulsion Systems," *67. Deutscher Luft- und Raumfahrtkongress DLRK 2018*, Sept. 2018, Paper 480227.
https://doi.org/10.25967/480227

[31] Ludowicy, J., Rings, R., Finger, D. F., and Braun, C., "Sizing Studies of Light Aircraft with Serial Hybrid Propulsion Systems," *67. Deutscher Luft- und Raumfahrtkongress DLRK 2018*, Sept. 2018, Paper 480226.
https://doi.org/10.25967/480226

[32] Finger, D. F., Braun, C., and Bil, C., "Comparative Assessment of Parallel-Hybrid-Electric Propulsion Systems for Four Different Aircraft," *Journal of Aircraft*, Vol. 57, No. 5, 2020, pp. 843–853.
https://doi.org/10.2514/1.C035897

[33] Finger, D. F., Braun, C., and Bil, C., "Case Studies in Initial Sizing for Hybrid-Electric General Aviation Aircraft," *AIAA/IEEE Electric Aircraft Technologies Symposium (EATS)*, AIAA Paper 2018-5005, July 2018.
https://doi.org/10.2514/6.2018-5005

[34] Finger, D. F., Götten, F., Braun, C., and Bil, C., "Mass, Primary Energy, and Cost—The Impact of Optimization Objectives on the Initial Sizing of Hybrid-Electric General Aviation Aircraft," *CEAS Aeronautical Journal*, Vol. 11, 2020, pp. 713–730.
https://doi.org/10.1007/s13272-020-00449-8

[35] Finger, D. F., Braun, C., and Bil, C., "Initial Sizing for a Family of Hybrid-Electric VTOL General Aviation Aircraft," *67: Deutscher Luft- und Raumfahrtkongress DLRK 2018*, Sept. 2018, Paper 480102.
https://doi.org/10.25967/480102

[36] Hoogreef, M. F. M., Vos, R., de Vries, R., and Veldhuis, L. L. M., "Conceptual Assessment of Hybrid Electric Aircraft with Distributed Propulsion and Boosted Turbofans," *2019 AIAA Aerospace Sciences Meeting*, AIAA Paper 2019-1807, Jan. 2019.
https://doi.org/10.2514/6.2019-1807

[37] Hoogreef, M. F. M., de Vries, R., Sinnige, T., and Vos, R., "Synthesis of Aero-Propulsive Interaction Studies Applied to Conceptual Hybrid-Electric Aircraft Design," *AIAA Scitech 2020 Forum*, AIAA Paper 2020-0503, Jan. 2020.
https://doi.org/10.2514/6.2020-0503

[38] Orefice, F., Della Vecchia, P., Ciliberti, D., and Nicolosi, F., "Aircraft Conceptual Design Including Powertrain System Architecture and Distributed Propulsion," *AIAA Propulsion and Energy 2019 Forum*, AIAA Paper 2019-4465, Aug. 2019.
https://doi.org/10.2514/6.2019-4465

[39] Silva, H. L., and Guimarães, T. A. M., "Conceptual Design of a Thin-Haul Aircraft by Energy Sizing Optimization Including Aero-Propulsive Interactions," *AIAA Scitech 2020 Forum*, AIAA Paper 2020-1503, Jan. 2020.
https://doi.org/10.2514/6.2020-1503

[40] *National Academies of Sciences, Engineering, and Medicine, Commercial Aircraft Propulsion and Energy Systems Research: Reducing Global Carbon Emissions*, National Academies Press, Washington, DC, 2016.
https://doi.org/10.17226/23490

[41] Finger, D. F., Götten, F., Braun, C., and Bil, C., "On Aircraft Design Under the Considerationof Hybrid-Electric Propulsion Systems," *Proceedings of the 2018 Asia-Pacific International Symposium on Aerospace Technology (APISAT 2018)*, Springer, Singapore, 2019, pp. 1261–1272.
https://doi.org/10.1007/978-981-13-3305-7_99

[42] de Vries, R., Hoogreef, M., and Vos, R., "Preliminary Sizing of a Hybrid-Electric Passenger Aircraft Featuring Over-the-Wing Distributed-Propulsion," *2019 AIAA Aerospace Sciences Meeting*, AIAA Paper 2019-1811, Jan. 2019.
https://doi.org/10.2514/6.2019-1811

[43] Finger, D. F., Braun, C., and Bil, C., "A Review of Configuration Design for Distributed Propulsion Transitioning VTOL Aircraft," *Asia-Pacific International Symposium on Aerospace Technology—APISAT2017*, Oct. 2017.

[44] Ko, A., Schetz, J. A., and Mason, W. H., "Assessment of the Potential Advantages of Distributed-Propulsion for Aircraft," *XVI International Symposium on Air Breathing Engines (ISABE)*, AIAA Paper 2003-1094, Aug.–Sept. 2003.

[45] Jackson, P., *Jane's All the World's Aircraft: Development & Production 2017-2018*, IHS Markit, Coulsdon, England, U.K., 2017.
[46] Hofmann, J., Stumpf, E., Weintraub, D., Köhler, J., Pham, D., Schneider, M., Dickhoff, J., Burkhart, B., Reiner, G., Spiller, M., and Werner, E. A., "A Comprehensive Approach to the Assessment of a Hybrid Electric Powertrain for Commuter Aircraft," *AIAA Aviation Forum 2019*, AIAA Paper 2019-3678, June 2019. https://doi.org/10.2514/6.2019-3678
[47] *Logistic, Pilot's Operating Handbook Including the LBA Approved Airplane Flight Manual—Dornier 228-100*, Dornier GmbH, Munich, 1983.
[48] "Dornier 228 Advanced Commuter (AC) Facts & Figures," RUAG Aerospace Services GmbH, Wessling, Germany, 2015.
[49] TPE331-10 Turboprop Engine Brochure, Honeywell Aerospace, Phoenix, TX, 2016.
[50] "RUAG (Dornier) 228 NG," Jane's All the World's Aircraft: Development & Production, IHS Markit, 23 Jan. 2019, https://janes.ihs.com/JAWADevelopmentProduction/Display/jawaa704-jawa [retrieved 7 Nov. 2019].
[51] *Annex 6, Operation of Aircraft, Part I: International Commercial Air Transport— Aeroplanes*, International Civil Aviation Organization, Montreal, 2016.
[52] Hoerner, S. F., *Fluid-Dynamic Drag*, Hoerner Fluid Dynamics, Bricktown, NJ, 1965, Chaps. VIII, XIII.
[53] Götten, F., Havermann, M., Braun, C., Gómez, F., and Bil, C., "On the Applicability of Empirical Drag Estimation Methods for Unmanned Air Vehicle Design," *2018 Aviation Technology, Integration, and Operations Conference*, AIAA Paper 2018-3192, June 2018. https://doi.org/10.2514/6.2018-3192
[54] Götten, F., Finger, D. F., Marino, M., Bil, C., Havermann, M., and Braun, C., "A Review of Guidelines and Best Practices for Subsonic Aerodynamic Simulations using RANS CFD," *Asia-Pacific International Symposium on Aerospace Technology—APISAT 2019*, 2019.
[55] Hirsch, C., *Computational Methods for Inviscid and Viscous Flows*, Wiley, Chichester, England, U.K., Dec. 2002, Chap. 22.
[56] Schlichting, H., and Gersten, K., *Boundary-Layer Theory*, 9th ed., Springer, Berlin, 2017, Chap. 6.
[57] *Acceptable Means of Compliance and Guidance Material to Certification Specifications for Normal-Category Aeroplanes (CS-23)*, European Aviation Safety Agency, Cologne, Germany, 2017.
[58] *Standard Specification for Performance of Aeroplanes*, ASTM F3179/F3179M-16, ASTM International, West Conshohocken, PA, 2016.
[59] Jansen, R. H., Bowman, C., Jankovsky, A., Dyson, R., and Felder, J., "Overview of NASA Electrified Aircraft Propulsion Research for Large Subsonic Transports," *53rd AIAA/SAE/ASEE Joint Propulsion Conference*, AIAA Paper 2017-4701, July 2017. https://doi.org/10.2514/6.2017-4701
[60] Bruce, P. G., Freunberger, S. A., Hardwick, L. J., and Tarascon, J.-M., "Li–O2 and Li–S Batteries with High Energy Storage," *Nature Materials*, Vol. 11, 2012, pp. 19–29. https://doi.org/10.1038/nmat3191